Journal of Palaeogeography

ORIGINAL ARTICLE Open Access

Ooidal ironstones in the Meso-Cenozoic sequences in western Siberia: assessment of formation processes and relationship with regional and global earth processes

Maxim Rudmin[1*], Santanu Banerjee[2], Elshan Abdullayev[3], Aleksey Ruban[1], Ekaterina Filimonenko[1], Elena Lyapina[4], Roman Kashapov[1] and Aleksey Mazurov[1]

Abstract

This study investigates the process of formation of ooidal ironstones in the Upper Cretaceous-Paleogene succession in western Siberia. The formation of such carbonate-based ironstones is a continuing problem in sedimentary geology, and in this study, we use a variety of data and proxies assembled from core samples to develop a model to explain how the ooidal ironstones formed. Research on pyrite framboids and geochemical redox proxies reveals three intervals of oceanic hypoxia during the deposition of marine ooidal ironstones in the Late Cretaceous to the Early Paleogene Bakchar ironstone deposit in western Siberia; the absence of pyrite indicates oxic conditions for the remaining sequence. While goethite formed in oxic depositional condition, chamosite, pyrite and siderite represented hypoxic seawater. Euhedral pyrite crystals form through a series of transition originating from massive aggregate followed by normal and polygonal framboid. Sediments associated with goethite-chamosite ironstones, encompassing hypoxic intervals exhibit positive cerium, negative europium, and negative yttrium anomalies. Mercury anomalies, associated with the initial stages of hypoxia, correlate with global volcanic events. Redox sensitive proxies and ore mineral assemblages of deposits reflect hydrothermal activation. Rifting and global volcanism possibly induced hydrothermal convection in the sedimentary cover of western Siberia, and released iron-rich fluid and methane in coastal and shallow marine environments. This investigation, therefore, reveals a potential geological connection between Large Igneous Provinces (LIPs), marine hypoxia, rifting and the formation of ooidal ironstones in ancient West Siberian Sea.

Keywords: Ooidal ironstone, Pyrite framboids, Late Cretaceous, Early Paleogene, Western Siberia, Bakchar ironstone deposit, Redox conditions

1 Introduction

Ooidal ironstones represent non-siliceous sandy and clayey sediments consisting of at least 5% iron oolith/ooid and 15% iron (Young 1989; Petranek and Van Houten 1997), and form abundantly during the Ordovician-Devonian, the Jurassic-Cretaceous and the Paleogene (Van Houten and Bhattacharyya 1982; Van Houten and Arthur 1989; Young 1989) but are rare in modern sediments (Kimberley 1994; Heikoop et al. 1996; Sturesson et al. 2000). The origin of ooidal ironstones remains controversial as there is no unanimity amongst researchers regarding the source of iron. Several researchers considered that iron is available by the weathering of continents and it is delivered into the ocean by river or ground water (Strakhov 1947; Castano and Garrels 1950; Huber and Garrels 1953; Kholodov 2014). Others suggested submarine hydrothermal exhalative source of iron (Pavlov et al. 1991; Kimberley 1979, 1989, 1994; Pavlov 1996; Rudmin et al. 2019; Todd et al. 2019). Modern ooidal ironstones developed in the Mahengetang Island in Indonesia (Heikoop et al. 1996) support the "volcanogenic" hypothesis (Sturesson et al. 2000; Sturesson 2003). Proponents of the "exhalation" hypothesis consider

* Correspondence: rudminma@tpu.ru
[1]Division for Geology, School of Earth Sciences and Engineering, Tomsk Polytechnic University, 634050 Tomsk, Russia
Full list of author information is available at the end of the article

the transportation of hydrothermal Fe^{2+} along with phosphorus and manganese by anoxic seawater and upwelling of the same on oxygenated continental shelf (Todd et al. 2019). Subsequently the Fe^{2+} gets oxidized by biological or abiological ways resulting in formation of ooids and peloids (Dahanayake and Krumbein 1986; Burkhalter 1995; Taylor and Konhauser 2011; Todd et al. 2019). Several studies indicated that mineralogical and chemical compositions of ironstones implicate the mode of origin as well as depositional conditions influence (Van Houten and Purucker 1984; Maynard 1986; Kimberley 1989; Siehl and Thein 1989; Sturesson et al. 2000).

Recent investigations explore the relationship between periods of intense volcanism (Large Igneous Provinces, LIPs), global ocean anoxic events and the formation of ooidal ironstone deposits (Percival et al. 2015; Ernst and Youbi 2017; Scaife et al. 2017; Keller et al. 2018). Although Van Houten (1986) and Van Houten and Arthur (1989) indicated a relationship between ooidal ironstones and anoxic events, this is yet to be investigated thoroughly (Turgeon and Creaser 2008; Jenkyns 2010; Raven et al. 2018). While, the origin of the giant ironstone in the Meso-Cenozoic Bakchar deposit has been debated, but no study attempts to relate hypoxia, global volcanism and ironstone deposits, because the integration of data related to mineralogical and chemical composition of ironstones with proxies for redox and volcanism is still lacking.

The Bakchar ironstone deposit has been studied since 1960s, and the early studies have provided the overall geological structure from core data (Belous et al. 1964; Nikolaeva 1967). Subsequently Pavlov (1989) has proposed the origin of West Siberian iron ore basin by considering spatial association of ironstone deposits with oil and gas deposits. A detailed core drilling has made it possible for extensive studies on the origin of the ironstone (Podobina and Kseneva 2005; Asochakova 2014; Rudmin et al. 2014; Gnibidenko et al. 2015; Rudmin and Mazurov 2016).

The study of pyrite framboids is useful for determination of hypoxia during marine deposition (Wilkin et al. 1996; Wignall et al. 2005; Wei et al. 2015). Further, concentrations of trace metals such as molybdenum, vanadium, uranium are widely used as proxies for reflecting

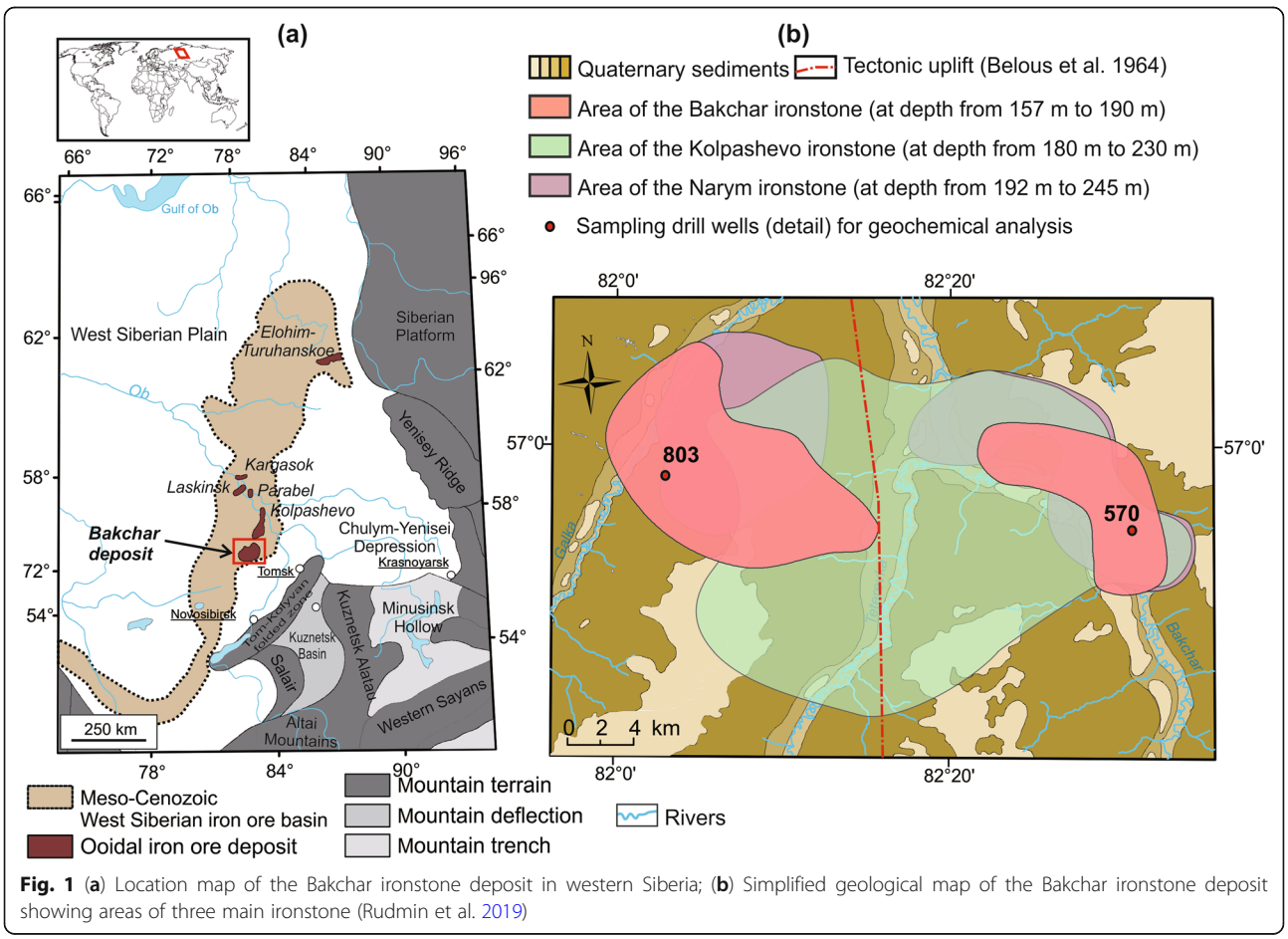

Fig. 1 (**a**) Location map of the Bakchar ironstone deposit in western Siberia; (**b**) Simplified geological map of the Bakchar ironstone deposit showing areas of three main ironstone (Rudmin et al. 2019)

depositional redox condition (Brumsack 2006; Tribovillard et al. 2006; Algeo and Tribovillard 2009; Lebedel et al. 2013). Mercury anomaly traces global volcanism in a few studies (Scaife et al. 2017; Sabatino et al. 2018; Them et al. 2019). An integrated study involving pyrite framboids, trace element concentrations and mercury anomaly of the Bakchar ironstone deposit is likely to provide a detailed perspective for establishing the relationship between hypoxia, global volcanism, rifting and the origin of ooidal ironstones. The aim of this work is to (1) infer the origin of iron in the Bakchar ironstone deposit in western Siberia; (2) understand variations in redox conditions across the ironstone deposit; and, (3) examine the relationship between LIPs, anoxia and the timing of ironstone formation. We assess redox conditions of the depositional setting based on several proxies including diameter of pyrite framboids, concentrations of trace elements and enrichment factors of these elements in available core samples across the Late Cretaceous-Early Paleogene section in Bakchar ironstone deposit. And on the basis of mercury anomalies in sediments, we attempt to record contemporary volcanic events.

2 Geological setting

The Bakchar ironstone deposit develops in the south-eastern part of western Siberia (52°01′45″N; 82°07′20″E) situated 200 km northwest of Tomsk (Fig. 1). The ironstone occurs as 150 km wide and about 2000 km long deposit in the West Siberian iron ore basin along eastern and south-eastern borders of the West Siberian Plate (Fig. 1a). This Upper Cretaceous-Palaeogene iron ore deposit occurs in subsurface at depth ranging from 165 m to 230 m (Belous et al. 1964; Podobina and Kseneva 2005; Lebedeva et al. 2013, 2017). The ore-bearing strata in Bakchar deposited in transgressive coastal and shallow marine environments, attaining a maximum thickness of 80 m (Fig. 2; references for shallow marine). The deposit occurs at the northern end of a Mesozoic dome, also known as Bakchar tectonic uplift (Belous et al. 1964; Rudmin et al. 2019). The gently dipping (less than 3°) ore horizons occur at the north-west and east of watershed axes of Rivers Galka and Bakchar. The roof of the upper ore horizon in Bakchar ironstone lies subsurface at the depth ranging from 157 m to 160 m at the western sector of the deposit, whereas at the eastern sector, the same deposit occurs at depth ranging from 170 m to 175 m.

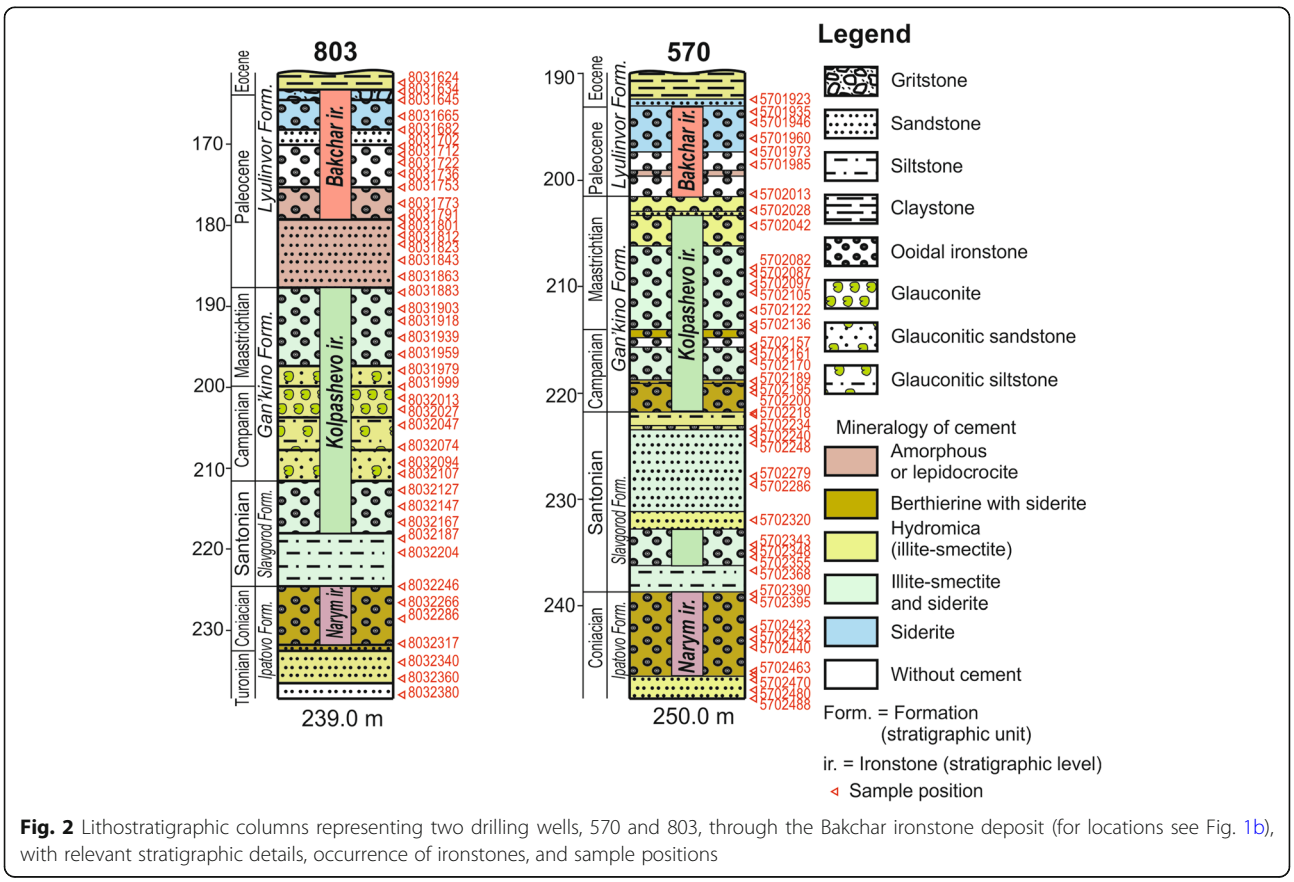

Fig. 2 Lithostratigraphic columns representing two drilling wells, 570 and 803, through the Bakchar ironstone deposit (for locations see Fig. 1b), with relevant stratigraphic details, occurrence of ironstones, and sample positions

Ooidal ores occur at three stratigraphic levels in this deposit, viz. the Narym, the Kolpashevo and the Bakchar (Fig. 2; Belous et al. 1964; Rudmin and Mazurov 2016; Rudmin et al. 2019). The Narym ironstone occurs at the top part of the Ipatovo Formation, which, in turn, overlies the Kuznetsovo Formation. The Ipatovo Formation consists of fine-grained sandstones and greyish-green siltstones with interlayers of clay that passes upward to the Narym ironstones. The Kolpashevo ironstones occur in association with glauconitic sandstones, siltstones and silty clays of the Santonian Slavgorod Formation and the Campanian-Maastrichtian Gan'kino Formation. The lower part of the Lyulinvor Formation consists of medium-grained sands and sandstones which pass upward to the Bakchar ironstones and claystones.

3 Materials and methods

Eighty-seven core samples were collected from the Bakchar ironstone deposit with an interval from 0.5 m to 2 m from two wells, 570 and 803 at eastern and western sectors respectively (Fig. 2). Core samples were powdered using an agate ball mill for geochemical studies. 68 thin sections were investigated for pyrite framboids by scanning electron microscope (SEM). Diameters of pyrite framboids were measured in polished sections using a TESCAN VEGA 3 SBU SEM equipped with an OXFORD X-Max 50 EDS analyzer and a Si/Li crystal detector. An accelerating voltage of 20 kV with a beam current between 3.5 nA and 15 nA was used for SEM observations. For each thin section, more than 100 pyrite framboids were measured primarily in backscatter mode.

Major element concentrations of the powdered samples were estimated by HORIBA XGT 7200 X-ray fluorescence microscope (XRF) operated at a tube current of 1 mA, beam diameter of 1.2 mm, and a voltage of 50 kV. Fused pellets were prepared by pressing and melting sample powder for analysis using XRF. The detection limit for major elements was better than 0.01 wt.%.

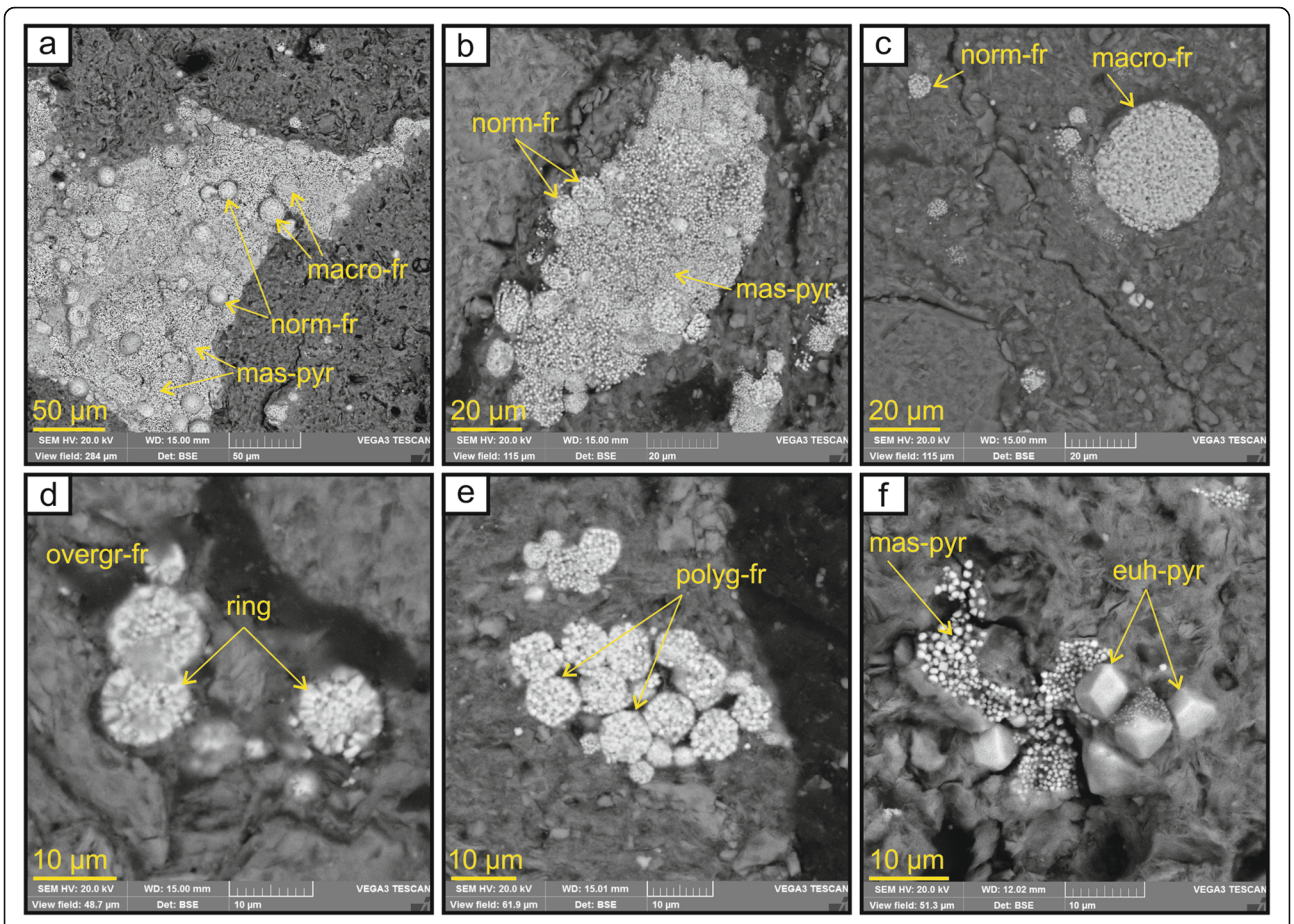

Fig. 3 SEM images showing different morphological forms of pyrite in Bakchar ironstone deposit. (**a**) A huge aggregate of massive pyrite (mas-pyr) with normal framboids (norm-fr) and macro framboids (macro-fr) in sample 5702189; (**b**) Nodule of massive pyrite with normal framboids in sample 8032047; (**c**) Macro framboid and normal framboids in cement in sample 8032360; (**d**) Overgrowth or annular framboids (overgr-fr) in sample 5702195; (**e**) Polygonal framboids (polyg-fr) in sample 5702286; (**f**) Massive and euhedral (euh-pyr) pyrite in sample 5702189

Table 1 Statistical parameters of pyrite framboids from three intervals in well 570 (size in μm)

Sample	Age	Mean diameter	Standard deviation	Minimal	Maximum	Median diameter	First quartile (25%)	Third quartile (75%)
5702157	Campanian	11.3	5.2	3.1	25.7	10.4	7.3	15.9
5702161	Campanian	7.1	5.9	2.7	26.4	5.2	3.7	7.1
5702170	Campanian	6.8	4.1	2.8	27.6	5.8	4.9	7.4
5702189	Campanian	7.2	3.3	2.5	19.4	6.0	4.7	8.6
5702218	Santonian	5.4	2.2	2.0	17.4	5.1	4.0	6.0
5702219	Santonian	8.0	5.1	4.1	32.4	6.3	5.3	7.9
5702240	Santonian	6.3	2.3	1.4	19.3	5.9	4.7	7.5
5702248	Santonian	5.3	1.8	1.9	10.2	5.2	4.0	6.3
5702279	Santonian	5.7	2.4	1.2	11.1	5.3	3.9	6.8
5702286	Santonian	5.7	2.7	2.5	24.0	5.2	4.4	6.4
5702320	Santonian	5.5	2.3	2.2	19.7	5.0	4.1	6.3
5702343	Santonian	5.1	1.9	2.3	15.2	4.6	3.8	5.9
5702348	Santonian	6.2	4.3	2.2	29.0	4.9	4.0	6.7
5702368	Santonian	6.7	3.0	1.4	18.7	6.0	4.7	7.8
5702390	Coniacian	6.4	3.0	3.4	13.1	5.7	4.8	6.7
5702432	Coniacian	6.7	3.0	2.6	17.7	6.3	5.0	7.3
5702440	Coniacian	12.0	8.5	2.9	46.4	7.6	5.9	17.2
5702465	Coniacian	9.6	3.8	3.5	19.3	8.5	6.8	12.1

Concentrations of trace elements (TEs), including rare earth elements (REEs), were estimated using inductively coupled plasma-mass spectrometry (ICP-MS) at the Hydrogeochemistry Research Laboratory, Tomsk Polytechnic University. About 0.5 g of powdered sample was fused using 0.8 g of $LiBO_2/Li_2B_4O_7$ at 1050 °C for about 15 min. The glass beads were dissolved in a mixture of 5:4:1.5 HF, HNO_3, and $HClO_4$ at 120 °C in a platinum crucible for 6 h. The acid mixture was allowed to evaporate at 160 °C. The sample residue was dissolved in 10 ml of $5HNO_3$. The resultant solutions were filtered and analyzed for REEs (see El-Habaak et al. 2016). Elemental concentrations were normalized to Al content to remove the effect of variable terrigenous input (Brumsack 2006; Tribovillard et al. 2006). Enrichment factor (EF) was calculated for each sample following Tribovillard et al. (2006). The Al EF was calculated as: $\text{Al EF} = \text{Al}_{\text{Sample}}/\text{Al}_{\text{PAAS}}$. While EF values exceeding 1 represent a detectable enrichment of the element above the average shale concentration, those in excess of 10 indicate a moderate to strong enrichment (Tribovillard et al. 2006, 2012; Núñez-Useche et al. 2016).

Pyrolysis was performed on samples using a model 6 turbo ROCK-EVAL analyzer (Vinci Technologies) at the Arctic Seas Carbon Research International Laboratory, Tomsk Polytechnic University. Around 100 mg samples were heated initially at 300 °C to release volatile hydrocarbons, and subsequently at 600 °C to release pyrolytic hydrocarbons. The CO/CO_2 released

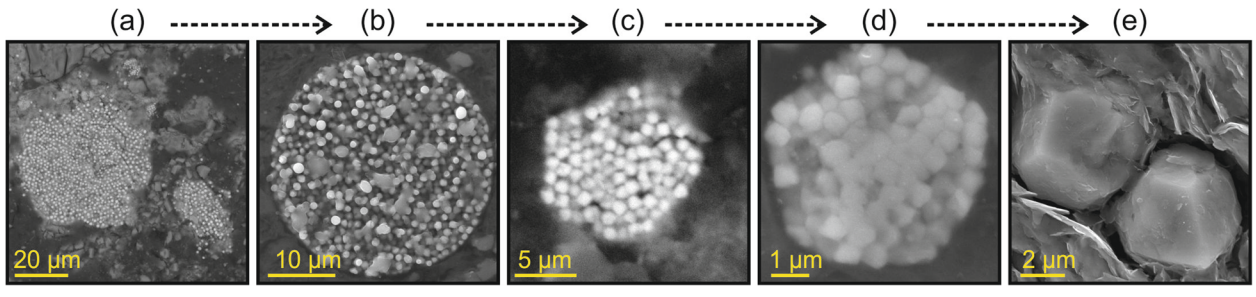

Fig. 4 SEM images showing evolutionary series of pyrite formation from framboid to euhedral crystal: (**a**) Massive pyrite microcrystals; (**b**) Normal framboids; (**c**, **d**) Polygonal framboids; (**e**) Euhedral pyrite crystal

during the analysis was registered with infra-red source cell detector to quantify the total organic carbon content (TOC). Mercury concentrations were measured using 50 mg of powdered sample with a Lumex RA-915 Portable Mercury Analyzer fitted to the PYRO-915 Pyrolyzer.

4 Results

4.1 Morphology and size distribution of pyrite framboids

Pyrite occurs as various forms including framboids (Fig. 3a–e), irregular and subhedral masses (Fig. 3a, b), and euhedral crystals (Fig. 3f). The last variety of pyrite is the least abundant. Pyrite framboids are further divided into several types, such as normal, macro, overgrowth and polygonal (Fig. 3; cf. Sawlowicz 1993; Wei et al. 2015). Mean diameter, standard deviation and other statistical parameters for normal pyrite framboids are presented in Table 1.

Normal framboids (Fig. 3a–c) appear as regular spheres with diameters varying from 2 μm to 20 μm.

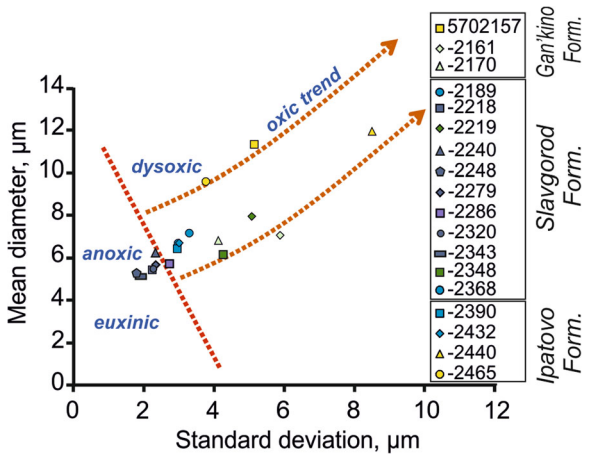

Fig. 5 Cross plot between mean diameter and standard deviation of pyrite framboids. Oxic-anoxic field boundaries are adapted on the basis of published data (cf. Wilkin et al. 1996; Bond and Wignall 2010; Merinero and Cárdenes 2018). Most of the samples of the Slavgorod Formation plot within the anoxic field. *Form.* = Formation

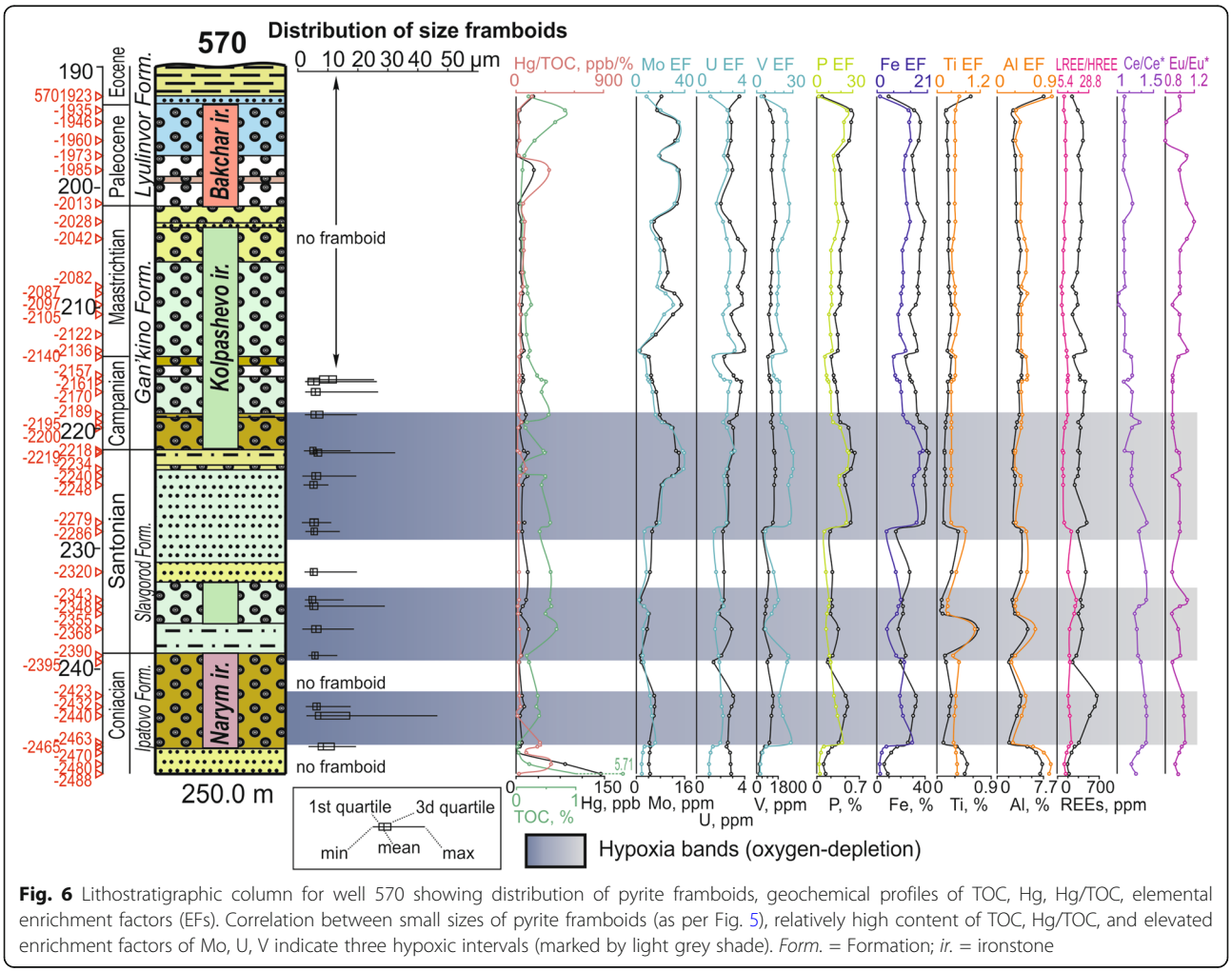

Fig. 6 Lithostratigraphic column for well 570 showing distribution of pyrite framboids, geochemical profiles of TOC, Hg, Hg/TOC, elemental enrichment factors (EFs). Correlation between small sizes of pyrite framboids (as per Fig. 5), relatively high content of TOC, Hg/TOC, and elevated enrichment factors of Mo, U, V indicate three hypoxic intervals (marked by light grey shade). *Form.* = Formation; *ir.* = ironstone

Table 2 Major oxides for samples of two sections in wells 570 and 803 from eastern and western (respectively) corners of the Bakchar ironstone deposit

Well	Samples	Depth from, m	Depth to, m	SiO_2, %	Al_2O_3, %	TiO_2, %	$Fe_2O_{3(Total)}$, %	MgO, %	CaO, %	Na_2O, %	K_2O, %	MnO, %	P_2O_5, %
570	5701923	192.3	193.5	54.19	14.49	0.92	13.71	1.33	0.74	0.25	1.57	0.20	0.18
570	5701935	193.5	194.6	28.14	5.22	0.25	44.77	0.49	0.33	0.16	0.92	0.25	1.31
570	5701946	194.6	196.0	29.63	5.82	0.29	50.55	0.61	0.31	0.18	0.83	0.14	1.32
570	5701960	196.0	197.3	28.35	5.49	0.28	48.52	0.59	0.30	0.17	0.80	0.14	1.20
570	5701973	197.3	198.5	33.72	5.62	0.30	42.50	0.61	0.30	0.16	0.94	0.12	0.80
570	5701985	198.5	199.8	30.81	5.96	0.32	43.95	0.69	0.21	0.15	0.96	0.14	0.89
570	5701998	199.8	201.3	31.05	6.01	0.32	46.67	0.74	0.27	0.16	1.04	0.12	0.97
570	5702013	201.3	202.8	27.12	6.06	0.33	48.52	0.77	0.19	0.16	0.90	0.12	0.98
570	5702028	202.8	204.2	20.37	6.31	0.31	55.76	0.82	0.25	0.13	0.76	0.14	1.14
570	5702042	204.2	208.2	23.66	7.44	0.35	50.81	0.96	0.20	0.19	0.96	0.20	0.90
570	5702082	208.2	208.7	23.72	7.00	0.34	48.43	0.91	0.17	0.19	0.95	0.28	0.85
570	5702087	208.7	209.7	28.56	7.48	0.37	49.13	0.95	0.20	0.22	1.09	0.23	0.94
570	5702097	209.7	210.5	30.93	7.11	0.38	45.89	0.92	0.21	0.25	1.16	0.16	0.87
570	5702105	210.5	212.2	35.55	6.74	0.40	38.96	0.84	0.37	0.32	1.24	0.12	0.69
570	5702122	212.2	213.6	34.01	6.93	0.36	45.12	1.04	0.46	0.23	1.28	0.14	0.81
570	5702136	213.6	214.0	29.54	6.34	0.30	47.66	1.17	0.50	0.13	1.22	0.14	0.79
570	5702140	214.0	215.7	42.45	7.90	0.41	34.20	1.27	0.33	0.23	1.91	0.07	0.54
570	5702157	215.7	216.1	40.37	7.78	0.37	39.48	1.31	0.43	0.20	1.82	0.08	0.68
570	5702161	216.1	217.0	34.80	6.78	0.30	41.59	1.27	0.49	0.17	1.59	0.09	0.69
570	5702170	217.0	218.9	33.97	7.05	0.30	45.85	1.29	0.46	0.19	1.71	0.11	0.81
570	5702189	218.9	219.5	31.57	6.92	0.29	48.36	1.28	0.41	0.20	1.77	0.12	0.86
570	5702195	219.5	220.0	25.60	6.29	0.25	51.25	1.20	0.30	0.21	1.81	0.15	0.88
570	5702200	220.0	221.8	21.95	5.95	0.23	57.98	1.08	0.31	0.18	1.54	0.19	1.21
570	5702218	221.8	221.9	16.39	4.94	0.18	60.05	0.89	0.30	0.15	1.16	0.21	1.32
570	5702219	221.9	223.4	18.22	5.36	0.21	61.27	0.96	0.42	0.16	1.29	0.23	1.44
570	5702234	223.4	224.0	18.47	5.17	0.22	57.57	0.96	0.49	0.16	1.33	0.23	1.29
570	5702240	224.0	224.8	20.85	5.70	0.24	56.49	1.06	0.35	0.17	1.35	0.19	1.05
570	5702248	224.8	227.9	20.13	5.75	0.24	57.13	1.13	0.38	0.19	1.23	0.16	1.08
570	5702279	227.9	228.6	18.64	5.20	0.21	54.97	1.35	1.19	0.21	1.20	0.24	1.29
570	5702286	228.6	232.0	53.49	8.08	0.66	22.08	1.37	0.79	0.44	2.50	0.15	0.46
570	5702320	232.0	234.3	35.05	7.50	0.41	38.76	1.66	0.83	0.28	2.16	0.21	0.61
570	5702343	234.3	234.8	50.29	4.63	0.13	29.99	1.14	0.41	0.13	2.05	0.07	0.54
570	5702348	234.8	235.5	51.56	5.51	0.16	31.32	1.31	0.48	0.16	2.23	0.07	0.58
570	5702355	235.5	236.8	48.38	5.77	0.17	30.14	1.39	0.49	0.17	2.24	0.06	0.52
570	5702368	236.8	239.0	46.18	10.06	1.12	26.22	1.60	1.77	0.19	1.45	0.12	0.81
570	5702390	239.0	239.5	44.50	4.69	0.22	34.95	1.10	0.95	0.21	1.15	0.12	0.58
570	5702395	239.5	242.3	53.94	3.83	0.25	27.28	0.87	0.72	0.16	1.17	0.07	0.42
570	5702423	242.3	243.2	27.26	7.50	0.41	46.32	1.42	1.36	0.26	0.79	0.15	1.13
570	5702432	243.2	244.0	31.88	7.02	0.37	45.78	1.29	1.32	0.25	0.85	0.15	1.15
570	5702440	244.0	246.3	35.27	6.08	0.31	43.31	1.13	1.21	0.22	0.88	0.14	1.07
570	5702463	246.3	246.5	40.23	3.97	0.19	36.82	0.77	0.94	0.17	0.90	0.12	0.81
570	5702465	246.5	247.0	52.12	9.63	0.54	23.91	1.24	0.91	0.71	1.53	0.08	0.58
570	5702470	247.0	248.0	57.16	12.33	0.70	16.68	1.47	0.86	0.97	1.83	0.06	0.43

Table 2 Major oxides for samples of two sections in wells 570 and 803 from eastern and western (respectively) corners of the Bakchar ironstone deposit *(Continued)*

Well	Samples	Depth from, m	Depth to, m	SiO_2, %	Al_2O_3, %	TiO_2, %	$Fe_2O_{3(Total)}$, %	MgO, %	CaO, %	Na_2O, %	K_2O, %	MnO, %	P_2O_5, %
570	5702480	248.0	248.8	59.50	14.19	0.84	9.07	1.64	0.78	1.22	2.05	0.00	0.25
570	5702488	248.8	250.0	59.67	13.69	0.79	13.06	1.58	0.84	1.11	1.98	0.05	0.35
803	8031624	162.4	163.4	16.08	5.36	0.28	56.16	0.91	1.80	0.20	0.51	0.35	1.63
803	8031634	163.4	164.5	18.67	4.86	0.24	58.56	0.52	0.36	0.05	0.66	0.26	1.43
803	8031645	164.5	166.5	18.80	5.19	0.32	55.03	0.86	0.98	0.05	1.31	0.43	1.23
803	8031665	166.5	168.2	15.18	4.32	0.23	61.54	0.50	0.41	0.04	0.49	0.28	1.37
803	8031682	168.2	170.2	76.66	5.60	0.35	10.37	0.38	0.56	0.08	1.26	0.05	0.21
803	8031702	170.2	171.2	18.22	5.42	0.27	62.61	0.55	0.24	0.08	0.61	0.17	1.45
803	8031712	171.2	172.2	18.92	5.53	0.26	62.82	0.57	0.26	0.09	0.65	0.17	1.43
803	8031722	172.2	173.6	19.10	5.45	0.27	61.38	0.59	0.25	0.08	0.69	0.17	1.42
803	8031736	173.6	175.3	20.72	5.73	0.28	59.98	0.62	0.26	0.16	0.77	0.17	1.33
803	8031753	175.3	177.3	37.24	6.42	0.34	45.29	0.74	0.27	0.18	1.50	0.12	0.96
803	8031773	177.3	179.1	43.13	5.84	0.26	39.65	0.76	0.24	0.44	1.85	0.10	0.88
803	8031791	179.1	180.1	56.47	6.17	0.31	27.58	0.73	0.23	0.20	2.39	0.07	0.62
803	8031801	180.1	181.2	64.44	6.62	0.40	20.75	0.70	0.25	0.66	2.54	0.06	0.20
803	8031812	181.2	182.3	53.39	6.99	0.37	26.64	0.78	0.28	0.58	2.26	0.07	0.44
803	8031823	182.3	184.3	57.28	5.83	0.37	24.19	0.66	0.24	0.49	2.24	0.06	0.32
803	8031843	184.3	186.3	43.60	6.04	0.27	36.89	0.83	0.23	0.50	2.05	0.09	0.25
803	8031863	186.3	188.3	52.88	6.74	0.32	27.08	0.99	0.32	0.50	2.64	0.06	0.34
803	8031883	188.3	190.3	48.32	6.88	0.33	31.48	1.09	0.26	0.22	2.52	0.08	0.64
803	8031903	190.3	191.8	44.38	6.99	0.34	33.47	1.34	0.88	0.13	2.69	0.08	0.34
803	8031918	191.8	193.9	36.90	6.75	0.33	40.43	1.17	0.43	0.15	1.66	0.09	0.76
803	8031939	193.9	195.9	45.86	7.12	0.37	32.75	1.34	0.50	0.16	2.45	0.07	0.41
803	8031959	195.9	197.9	41.36	9.90	0.50	32.87	1.72	0.65	0.18	2.49	0.05	0.44
803	8031979	197.9	199.9	51.30	9.62	0.52	22.40	1.53	0.79	0.18	2.85	0.07	0.37
803	8031999	199.9	201.3	48.66	10.22	0.36	22.49	2.25	0.50	0.15	4.42	0.04	0.37
803	8032013	201.3	202.7	48.86	10.25	0.36	23.60	2.29	0.40	0.16	4.91	0.03	0.25
803	8032027	202.7	204.7	59.20	12.57	0.53	12.60	2.06	0.61	0.57	3.51	0.02	0.08
803	8032047	204.7	207.4	55.33	10.86	0.40	15.58	2.27	0.59	0.46	4.04	0.02	0.12
803	8032074	207.4	209.4	55.77	10.04	0.39	17.87	2.06	0.60	0.16	3.79	0.02	0.32
803	8032094	209.4	210.7	53.10	7.53	0.37	21.42	1.47	0.51	0.51	2.72	0.04	0.08
803	8032107	210.7	212.7	43.97	5.72	0.28	33.31	1.50	0.87	0.27	1.94	0.25	0.23
803	8032127	212.7	214.7	48.48	5.27	0.22	31.37	1.23	1.09	0.20	1.85	0.12	0.07
803	8032147	214.7	216.7	47.27	5.09	0.22	31.45	1.41	1.11	0.34	1.72	0.17	0.17
803	8032167	216.7	218.7	53.76	6.62	0.30	25.01	1.45	0.80	0.08	2.42	0.10	1.12
803	8032187	218.7	220.4	55.05	8.47	0.44	20.56	1.49	1.38	0.05	2.30	0.11	0.62
803	8032204	220.4	224.6	58.45	5.07	0.21	21.45	1.47	0.74	0.23	2.70	0.04	0.34
803	8032246	224.6	226.6	42.82	6.28	0.33	34.81	1.04	1.28	0.18	1.56	0.11	0.39
803	8032266	226.6	228.6	51.47	4.05	0.22	33.83	0.84	0.81	0.40	1.73	0.12	0.30
803	8032286	228.6	231.7	57.28	4.00	0.22	28.69	0.83	0.80	0.16	2.43	0.10	0.50
803	8032317	231.7	234.0	67.99	4.31	0.25	16.81	0.92	0.65	0.15	0.08	0.06	0.44
803	8032340	234.0	236.0	64.48	4.19	0.21	18.07	1.08	0.94	0.20	1.48	0.07	0.30
803	8032360	236.0	238.0	64.96	4.65	0.23	18.29	1.12	0.85	0.26	1.50	0.07	0.30

Table 2 Major oxides for samples of two sections in wells 570 and 803 from eastern and western (respectively) corners of the Bakchar ironstone deposit *(Continued)*

Well	Samples	Depth from, m	Depth to, m	SiO_2, %	Al_2O_3, %	TiO_2, %	$Fe_2O_{3(Total)}$, %	MgO, %	CaO, %	Na_2O, %	K_2O, %	MnO, %	P_2O_5, %
803	8032380	238.0	239.0	74.75	6.15	0.43	7.55	0.74	0.83	0.58	2.19	0.03	0.32

Each framboid consists of numerous microcrystals, the diameter of which varies from 0.7 μm to 1.3 μm. The diameter of macro-framboids (Fig. 3a, c) varies from 21 μm to 60 μm. The diameter of octahedral to dodecahedral micro-crystals within macro-framboids may be up to 2 μm. The overgrowth (also known as annular) variety of framboids may exhibit a distinctive outer ring of elongated crystals (Fig. 3d; cf. Merinero et al. 2009, 2017; Merinero and Cárdenes 2018). The diameter of this rare variety of framboids varies from 6 μm to 20 μm. The polygonal framboid often consists of densely-packed microcrystals and has long dimension varied from 5 μm to 12 μm (Fig. 3e). Pyrite also occurs as massive aggregates consisting of tiny crystals (Fig. 3a, b, f). Diameter of individual crystal in these aggregates varies from 0.5 μm to 1.0 μm. Euhedral pyrite may occur either as solitary crystal or as clusters; pyrite in these clusters often exhibits dodecahedral form with average long dimension up to 10 μm (Figs. 3f and 4e).

Normal framboids with size varying from 2 μm to 20 μm, with a geometric mean of 6.1 μm, appear to be the first formed pyrite. The aggregation of iron sulfide microcrystals or the crystallization from sulfide-saturated colloids forms normal framboids (Berner 1984). The filling of the intercrystalline space in normal framboids with ferrisulfide and subsequent recrystallization possibly forms euhedral pyrites (cf. Zhao et al. 2018). Thus, the evolution of the pyrite reflects a transition from normal framboid to euhedral crystal through polygonal variety (Fig. 4).

Small pyrite framboids occur within shale, siltstone and ironstone beds in the three intervals in well 570 corresponding to the middle Coniacian, the Santonian and the early Campanian ages (Figs. 5 and 6). The average diameter of normal framboids in these intervals varies from 5.1 μm to 12.0 μm. The Santonian interval exhibits the smallest pyrite framboid with an average diameter of 5.6 μm (standard deviation: 2.5 μm) (Table 1). The mean diameter of framboids in the Coniacian and Campanian intervals varies from 6.4 μm to 12.0 μm (Fig. 5). Pyrite framboid does not occur in the Maastrichtian and Paleocene formations.

The occurrence of small variety of pyrite framboids in the three intervals in well 570 indicates oxygen-depleted depositional conditions (cf. Berner 1984; Wilkin et al. 1996; Wei et al. 2015; Merinero et al. 2017; Rickard 2019). The abundance and size of framboids indicate their formation in the hydrogen sulfide-rich bottom water column. The cross plot between mean diameter and standard deviation of framboids further indicates anoxic depositional conditions for two intervals: one at the lower part of the Slavgorod Formation and another encompassing the upper part of the Slavgorod Formation and the bottom part of the Gan'kino Formation (Figs. 5 and 6). Fe mineral assemblage for these intervals consists of chamosite peloids and ooids, siderite microcrystals and pyrite framboids. Rare authigenic minerals include barite and galena. Statistical parameters of pyrite framboids indicate dysoxic depositional condition for the lower part of the Ipatovo Formation (Figs. 5 and 6). Mineral assemblage of this interval comprises chamosite ooids and peloids, siderite-berthierine cement and pyrite besides rare pyrrhotite, barite, galena, sphalerite and arsenopyrite. Pyrite framboids less often occur within siltstone-claystone interlayers in the Lyulinvor Formation hosting the Bakchar ironstones.

4.2 Geochemistry

Concentrations of major and trace elements of ironstones and associated rocks are provided in Tables 2, 3, 4, and 5. Variations in trace element enrichment factors across the stratigraphic succession are provided in Figs. 6 and 7. While Mo, U, and V are proxies for sedimentary redox conditions, concentrations of P relate to primary productivity in marine environments, and contents of Ti and Zr indicate clastic influx (Brumsack 2006; Tribovillard et al. 2006; Algeo and Tribovillard 2009; Lebedel et al. 2013).

High values of enrichment factors (EFs) coincide with three hypoxic intervals containing small diameter of pyrite framboids in the lithostratigraphic column of well 570 (Fig. 6). Both Mo EF and V EF are higher than the median (10.9 and 18.2, respectively) in the lower and upper hypoxic intervals in well 570 (Fig. 6). U EF (from 2.1 to 3.3) in these intervals is higher relative to the rest of the sedimentary sequence in well 570 (Fig. 6). P EF has several peaks, which are synchronous with Fe EFs. P EF correlates positively with Fe EF ($r^2 = 0.8$). Values of both P EF and Fe EF are higher within ironstone intervals than the rest of the sequence (Figs. 6 and 7). High values

Table 3 Trace elements for samples of two sections in wells 570 and 803 from eastern and western (respectively) corners of the Bakchar ironstone deposit

Well	Samples	V, ppm	Cr, ppm	Co, ppm	Cu, ppm	Zn, ppm	Mo, ppm	Ba, ppm	Hf, ppm	Pb, ppm	Th, ppm	U, ppm
570	5701923	576	202	30	13	194	8.3	322	2.9	49.9	3.9	3.5
570	5701935	1152	286	23	14	175	7.2	180	1.6	57.6	11.4	2.7
570	5701946	1400	302	35	18	190	14.0	170	1.5	57.0	14.0	2.9
570	5701960	1344	290	34	17	185	13.1	161	1.4	54.7	13.3	2.8
570	5701973	1248	269	33	11	175	7.5	170	2.0	61.4	12.4	2.6
570	5701985	1248	259	32	12	204	14.0	189	1.8	64.3	16.2	3.0
570	5701998	1344	355	30	13	194	14.0	180	1.8	23.0	15.2	2.2
570	5702013	1536	403	33	10	185	13.1	180	1.7	27.8	17.1	2.0
570	5702028	1536	422	36	12	204	5.4	142	1.8	38.4	17.1	2.8
570	5702042	1248	384	35	13	185	10.3	142	2.0	42.2	16.2	4.0
570	5702082	1152	326	36	17	185	8.5	142	2.1	21.1	13.3	3.4
570	5702087	1200	380	36	17	205	12.6	170	2.3	39.5	18.0	3.8
570	5702097	1152	403	33	15	214	15.0	180	2.3	54.7	20.9	3.8
570	5702105	1056	355	32	17	185	10.3	170	1.9	9.6	16.2	2.9
570	5702122	1300	390	37	14	185	6.1	155	2.1	27.0	16.5	3.6
570	5702136	1440	394	38	9	175	1.0	123	2.0	42.2	15.2	4.0
570	5702140	931	288	28	18	214	4.0	189	1.7	16.3	13.3	2.2
570	5702157	1135	360	32	14	200	4.9	175	2.0	28.5	15.0	3.1
570	5702161	1248	403	33	8	175	5.1	142	2.0	38.4	15.2	3.7
570	5702170	1300	375	37	10	200	6.6	160	2.1	40.0	14.5	3.6
570	5702189	1300	330	40	12	220	7.7	170	2.2	40.0	12.9	3.4
570	5702195	1248	230	44	14	252	9.3	180	2.1	38.4	9.3	2.7
570	5702200	1400	250	48	16	235	12.0	175	1.9	30.5	10.4	3.1
570	5702218	1440	250	48	15	204	13.1	152	1.5	20.2	10.5	3.1
570	5702219	1550	230	53	15	195	14.5	160	1.9	24.0	11.0	3.0
570	5702234	1536	192	54	13	175	14.0	152	2.0	25.9	10.5	2.6
570	5702240	1536	202	56	18	185	12.2	123	1.6	28.8	12.4	2.6
570	5702248	1440	221	52	15	175	8.5	104	1.5	16.3	9.0	2.7
570	5702279	1344	188	56	12	311	6.8	133	2.0	44.2	13.3	2.6
570	5702286	442	76	36	20	214	3.7	218	2.5	23.0	10.5	2.2
570	5702320	1056	144	58	16	282	4.2	161	2.4	37.4	13.3	2.3
570	5702343	806	240	26	5	136	0.7	123	1.1	36.5	6.8	2.2
570	5702348	765	230	30	6	145	2.4	145	1.3	38.0	7.3	2.1
570	5702355	662	202	32	7	146	3.8	152	1.3	36.5	7.0	1.8
570	5702368	634	115	47	30	262	3.5	256	2.5	26.9	13.3	2.9
570	5702390	1152	288	28	5	185	1.8	170	1.6	25.9	9.5	1.9
570	5702395	922	250	20	2	146	1.7	161	1.1	24.0	8.0	1.3
570	5702423	1344	202	56	20	282	5.9	218	2.4	38.4	17.1	3.0
570	5702432	1325	218	51	17	263	5.9	213	2.3	38.0	15.8	2.9
570	5702440	1250	225	43	13	235	5.5	195	2.0	36.0	13.6	2.7
570	5702463	1056	230	27	4	175	4.3	152	1.4	30.7	8.7	2.0
570	5702465	640	163	25	19	195	4.6	245	2.3	24.5	8.7	2.6
570	5702470	410	125	23	27	203	4.5	288	2.6	20.8	8.4	2.8

Table 3 Trace elements for samples of two sections in wells 570 and 803 from eastern and western (respectively) corners of the Bakchar ironstone deposit *(Continued)*

Well	Samples	V, ppm	Cr, ppm	Co, ppm	Cu, ppm	Zn, ppm	Mo, ppm	Ba, ppm	Hf, ppm	Pb, ppm	Th, ppm	U, ppm
570	5702480	173	83	20	32	204	4.2	313	2.9	16.3	7.7	2.9
570	5702488	295	105	22	30	206	4.5	309	2.8	18.9	8.2	2.9
803	8031624	530	190	15	7	110	1.1	250	2.6	33.8	2.6	2.7
803	8031634	1600	330	36	5	160	8.9	70	1.5	33.0	16.0	3.4
803	8031645	1600	310	41	8	180	8.1	92	1.7	34.0	15.0	3.9
803	8031665	1300	280	31	4	180	1.9	99	1.4	33.0	14.0	3.0
803	8031682	1500	320	40	8	200	9.2	84	1.9	38.0	0.1	3.8
803	8031702	1400	310	35	5	190	8.8	120	2.0	36.0	0.1	3.6
803	8031712	1400	300	37	7	200	9.8	130	1.5	36.0	17.0	4.1
803	8031722	1500	340	39	10	200	0.4	150	2.2	35.0	18.0	3.6
803	8031736	1200	250	27	9	180	8.2	210	1.9	29.0	14.0	2.7
803	8031753	930	200	22	10	150	4.8	260	1.4	22.0	11.0	2.2
803	8031773	490	130	17	10	130	3.8	360	1.2	15.0	8.9	1.7
803	8031791	930	220	24	8	150	6.2	250	2.0	26.0	12.0	2.5
803	8031801	440	110	20	12	110	1.6	380	1.5	17.0	8.1	1.6
803	8031812	600	160	22	11	110	3.8	340	1.0	19.0	8.6	1.6
803	8031823	740	210	25	10	130	3.5	290	1.7	23.0	12.0	2.0
803	8031843	630	180	31	13	130	3.1	310	1.5	21.0	11.0	2.6
803	8031863	810	230	33	20	150	4.0	270	1.7	25.0	12.0	2.5
803	8031883	1300	420	31	9	150	6.0	140	2.2	36.0	17.0	3.2
803	8031903	1000	360	29	12	150	4.3	170	2.0	33.0	16.0	2.5
803	8031918	1200	310	30	8	160	5.5	140	1.6	34.0	16.0	2.5
803	8031939	1100	440	32	11	160	3.5	170	2.2	40.0	18.0	3.2
803	8031959	520	250	27	11	140	0.8	160	1.2	27.0	8.0	2.0
803	8031979	690	260	32	10	160	3.7	160	1.4	34.0	8.0	2.0
803	8031999	580	200	24	9	120	4.5	160	1.1	22.0	7.6	1.8
803	8032013	640	210	25	8	130	2.1	150	1.2	25.0	6.6	2.1
803	8032027	220	150	17	19	72	1.4	270	2.4	10.0	8.2	2.2
803	8032047	240	160	21	16	69	1.0	230	1.8	9.5	7.9	1.7
803	8032074	650	270	23	9	110	0.8	170	1.3	25.0	8.8	1.7
803	8032094	350	150	22	20	160	0.9	220	2.0	32.0	9.9	1.8
803	8032107	660	160	17	10	140	0.9	230	1.3	19.0	7.6	1.5
803	8032127	850	200	19	10	160	0.1	230	0.8	17.0	7.9	1.3
803	8032147	590	120	19	16	140	0.1	270	1.3	15.0	7.9	1.9
803	8032167	1900	310	46	15	250	16.0	280	1.8	42.0	17.0	4.4
803	8032187	1500	250	33	7	180	7.3	70	1.3	30.0	13.0	3.4
803	8032204	660	290	18	12	110	1.9	190	1.5	29.0	8.8	1.8
803	8032246	960	340	27	12	150	6.8	160	2.0	31.0	24.0	2.8
803	8032266	810	210	24	13	190	5.2	210	2.6	26.0	11.0	2.2
803	8032286	1010	220	27	8	240	6.0	150	1.5	27.0	9.6	2.0
803	8032317	840	220	22	9	220	4.4	200	1.1	25.0	8.6	1.5
803	8032340	670	190	21	13	150	2.6	360	1.6	28.0	9.4	2.1
803	8032360	800	240	31	16	180	2.4	300	1.6	30.0	9.3	2.0

Table 3 Trace elements for samples of two sections in wells 570 and 803 from eastern and western (respectively) corners of the Bakchar ironstone deposit *(Continued)*

Well	Samples	V, ppm	Cr, ppm	Co, ppm	Cu, ppm	Zn, ppm	Mo, ppm	Ba, ppm	Hf, ppm	Pb, ppm	Th, ppm	U, ppm
803	8032380	270	110	17	28	75	1.5	360	1.5	12.0	5.0	1.5

of EFs, especially the U EF, recognize two hypoxic intervals in well 803 (Fig. 7).

Concentrations of rare earth elements (REEs) vary from 124.5 ppm to 652.4 ppm (av. 348.7 ppm) in the Bakchar ironstone deposit. The ratio of light to heavy rare earth elements (LREE/HREE) varies from 5.4 to 28.8 with an average of 14.1. The hypoxic intervals exhibit positive Ce anomalies from 0.96 to 1.40. High values of Ce/Ce* (varying from 1.2 to 1.4) are characteristic for the Coniacian ooidal ironstones, the early Santonian siltstones and ooidal ironstones, the Campanian-Paleocene ooidal ironstones and glauconitic rocks. Eu anomalies range between 0.8 and 1.2 in the Bakchar ironstone deposit. Hypoxic intervals show negative Eu anomalies from 0.7 to 1.0. Most samples exhibit positive Ce and negative Eu anomalies in the Coniacian-lower Santonian rocks, accompanied by depletion in HREE (Fig. 8). Most ironstone samples show negative Y anomalies (Fig. 8), while those associated with siderite exhibit sharp negative Y anomalies. The top part of the Narym ironstone, the bottom part of the Santonian sandstones and the lower part of the siderite-goethite ore of the Bakchar ironstone exhibit negative Y anomalies up to 0.75 (Fig. 8).

The total organic carbon (TOC) content of rocks varies widely from 0.06 wt.% to 5.71 wt.% (Table 4; Figs. 6 and 7) within the Meso-Cenozoic Bakchar ironstone deposit. The TOC content is slightly higher (av. 0.36 wt.%) in sediments of the early Coniacian, the early Santonian, the early Campanian, and the late Paleocene-early Eocene (Figs. 6 and 7). The TOC content of the hypoxic intervals varies between 0.1 wt.% to 0.7 wt.%. However, the TOC content at the bottom part of the Ipatovo Formation is very high (5.7 wt.%). The Hg content varies from 1.8 ppb to 146.7 ppb (av. 38 ppb) in sediments; and varies between 4.0 ppb and 70.3 ppb within hypoxic intervals. High Hg content value (up to 110 ppb) characterizes the layer immediately below the hypoxic intervals in well 803 (Fig. 7). Hg concentrations and Hg/TOC values vary slightly from one well to another. Hg/TOC values are higher in sediments of the early Coniacian, the early Paleocene and the early Eocene in well 570; and in sediments of the late Turonian, the late Santonian, the Maastrichtian, the early Paleocene and the early Eocene in well 803 (Figs. 6 and 7).

5 Discussion

5.1 Hypoxia during the formation of ooidal ironstone deposit

Size of pyrite framboids as well as trace element enrichment factors distinguishes three hypoxic intervals within the Meso-Cenozoic Bakchar ironstone deposit (Figs. 6 and 7). Absence of pyrite framboids as well as the mineralogical assemblage dominated by goethite ooids with early diagenetic illite-smectite and lepidocrocite cement indicates oxic depositional conditions (Aller et al. 1986; Kimberley 1994; Heikoop et al. 1996; Sturesson et al. 2000; Di Bella et al. 2019) for the Maastrichtian and Paleocene intervals (Figs. 6 and 7; see also Rudmin et al. 2019). High values of Mo EF (above 11.3), U EF (above 2) and V EF (above 16.2) as well as occurrence of tiny (mean diameter < 6.3 μm) pyrite framboids indicate hypoxic shelf waters during the Coniacian (Figs. 5, 6, and 7). The Coniacian deposits encompass the time interval corresponding to OAE-2 (ocean anoxic event 2; Schlanger and Jenkyns 1976; Arthur et al. 1988; Jenkyns 2010). Widespread anoxic depositional condition during the Santonian results in the formation of tiny (mean diameter < 5.9 μm) pyrite framboids at the water column and/or on the sea floor (Figs. 5, 6, and 7). This Santonian hypoxic interval is marked by high values (from 11 to 28) of Mo EF, U EF, and V EF (Figs. 6 and 7), and corresponds to the OAE-3 known for the accumulation of organic-rich marine sediments (Wagreich 2012; Jones et al. 2018). The TOC content of sediments remains low notwithstanding the isolation of West Siberian Sea. Since P correlates well with Fe, the enhanced P EF indicates co-precipitation of chamosite and phosphate. A high iron flux possibly controls the precipitation of phosphorus in the form of phosphate-bearing rare earth elements. The lack of correlation between Fe EF and Ti EF and between Fe EF and Al EF (Figs. 6 and 7) rules out continental source of iron. Dysoxic bottom seawater promoted the formation of large framboids (mean diameter from 6.2 μm to 12.0 μm) and macro framboids (mean diameter from 20 μm to 46.4 μm) as well as large number of micro-aggregates of pyrite below the sediment-water interface during the early Coniacian and the late Campanian.

Bottoms of Kolpashevo and Bakchar ironstones in well 803 are marked by sharp swing in Mo EF, U EF and V EF (Fig. 7). Similar sharp swing in Mo EF and V EF (34.9 and 30.4 respectively) marks the Santonian hypoxic

Table 4 Enrichment factors (EFs), Hg, TOC and Hg/TOC for samples of two sections in wells 570 and 803 from eastern and western (respectively) corners of the Bakchar ironstone deposit

Well	Samples	Mo EF	U EF	V EF	P EF	Ti EF	Al EF	Fe EF	Hg, ppb	TOC, %	Hg/TOC
570	5701923	8.3	1.2	4.2	1.2	0.6	0.9	1.5	30.0	0.19	157.9
570	5701935	19.9	2.6	23.4	25.0	0.5	0.3	13.5	5.0	0.82	6.1
570	5701946	34.8	2.6	25.5	22.5	0.5	0.4	13.7	4.0	0.65	6.2
570	5701960	34.4	2.6	25.9	21.8	0.5	0.3	13.9	4.0	0.31	12.9
570	5701973	19.2	2.3	23.5	14.2	0.5	0.4	11.9	2.0	0.13	15.4
570	5701985	34.0	2.6	22.2	14.9	0.5	0.4	11.6	1.8	0.09	20.0
570	5701998	33.7	1.9	23.7	16.0	0.5	0.4	12.2	31.0	0.09	344.4
570	5702013	31.2	1.7	26.9	16.1	0.5	0.4	12.6	5.5	0.08	68.8
570	5702028	12.4	2.2	25.8	17.9	0.5	0.4	13.9	8.8	0.10	88.0
570	5702042	20.0	2.8	17.8	12.1	0.4	0.5	10.7	7.0	0.10	70.0
570	5702082	17.6	2.5	17.4	12.0	0.5	0.4	10.9	11.0	0.17	64.7
570	5702087	24.3	2.6	17.0	12.5	0.5	0.5	10.3	8.7	0.19	45.8
570	5702097	30.4	2.7	17.2	12.1	0.5	0.4	10.2	8.4	0.25	33.6
570	5702105	22.1	2.2	16.6	10.2	0.6	0.4	9.1	7.2	0.16	45.0
570	5702122	12.6	2.7	19.9	11.7	0.5	0.4	10.2	7.3	0.17	42.9
570	5702136	2.3	3.2	24.1	12.4	0.4	0.4	11.8	14.0	0.24	58.3
570	5702140	7.4	1.4	12.5	6.8	0.5	0.5	6.8	5.0	0.19	26.3
570	5702157	9.1	2.0	15.5	8.6	0.5	0.5	8.0	11.0	0.35	31.4
570	5702161	11.0	2.8	19.5	10.1	0.4	0.4	9.7	10.1	0.49	20.6
570	5702170	13.5	2.6	19.5	11.4	0.4	0.4	10.2	7.0	0.42	16.7
570	5702189	16.1	2.5	19.9	12.4	0.4	0.4	11.0	15.5	0.54	28.7
570	5702195	21.3	2.2	21.0	14.0	0.4	0.4	12.8	8.0	0.18	44.4
570	5702200	29.0	2.6	25.0	20.2	0.4	0.4	15.3	4.0	0.16	25.0
570	5702218	38.3	3.3	30.9	26.6	0.4	0.3	19.1	6.0	0.44	13.6
570	5702219	39.1	2.9	30.7	26.6	0.4	0.3	18.0	18.0	0.46	39.1
570	5702234	39.2	2.5	31.5	24.9	0.4	0.3	17.5	7.0	0.07	100.0
570	5702240	30.8	2.3	28.6	18.3	0.4	0.4	15.6	18.0	0.49	36.7
570	5702248	21.4	2.4	26.5	18.7	0.4	0.4	15.6	11.0	0.41	26.8
570	5702279	19.0	2.5	27.4	24.7	0.4	0.3	16.6	14.0	0.56	25.0
570	5702286	6.7	1.4	5.8	5.6	0.8	0.5	4.3	10.0	0.38	26.3
570	5702320	8.1	1.6	14.9	8.0	0.5	0.5	8.1	18.0	0.58	31.0
570	5702343	2.2	2.4	18.4	11.6	0.3	0.3	10.2	16.2	0.57	28.4
570	5702348	6.4	2.0	14.7	10.5	0.3	0.3	8.9	11.0	0.59	18.6
570	5702355	9.6	1.6	12.2	9.0	0.3	0.4	8.2	6.9	0.49	14.1
570	5702368	5.0	1.5	6.7	8.0	1.1	0.6	4.1	20.0	0.69	29.0
570	5702390	5.5	2.1	26.0	12.4	0.5	0.3	11.7	8.0	0.17	47.1
570	5702395	6.4	1.8	25.5	10.8	0.6	0.2	11.2	5.7	0.22	25.9
570	5702423	11.3	2.1	19.0	14.9	0.5	0.5	9.7	10.0	0.35	28.6
570	5702432	12.1	2.1	20.0	16.3	0.5	0.4	10.3	13.0	0.34	38.2
570	5702440	13.0	2.2	21.8	17.4	0.5	0.4	11.2	6.0	0.37	16.2
570	5702463	15.6	2.6	28.2	20.4	0.5	0.3	14.6	10.0	0.04	250.0
570	5702465	6.8	1.4	7.1	6.0	0.5	0.6	3.9	6.7	0.03	223.3
570	5702470	5.3	1.2	3.5	3.5	0.5	0.8	2.1	3.0	0.03	100.0

Table 4 Enrichment factors (EFs), Hg, TOC and Hg/TOC for samples of two sections in wells 570 and 803 from eastern and western (respectively) corners of the Bakchar ironstone deposit *(Continued)*

Well	Samples	Mo EF	U EF	V EF	P EF	Ti EF	Al EF	Fe EF	Hg, ppb	TOC, %	Hg/TOC
570	5702480	4.3	1.0	1.3	1.8	0.6	0.9	1.0	81.4	0.22	370.0
570	5702488	4.8	1.1	2.3	2.6	0.6	0.9	1.5	140.2	5.72	24.5
803	8031624	3.0	2.6	10.5	30.2	0.5	0.3	16.5	36.3	0.83	43.7
803	8031634	26.5	3.6	34.9	29.2	0.5	0.3	19.0	49.7	0.18	276.1
803	8031645	22.6	3.9	32.7	23.5	0.6	0.3	16.7	88.1	0.64	137.7
803	8031665	6.4	3.6	31.9	31.5	0.5	0.3	22.4	49.3	0.14	352.1
803	8031682	23.7	3.5	28.4	3.7	0.6	0.4	2.9	5.0	0.07	71.4
803	8031702	23.5	3.4	27.4	26.6	0.5	0.3	18.2	52.4	0.09	581.7
803	8031712	25.6	3.8	26.8	25.7	0.5	0.4	17.9	99.7	0.11	906.4
803	8031722	1.1	3.4	29.2	25.9	0.5	0.3	17.7	44.4	0.21	211.4
803	8031736	20.7	2.4	22.2	23.1	0.5	0.4	16.5	39.8	0.13	306.2
803	8031753	10.8	1.8	15.4	14.9	0.5	0.4	11.1	19.0	0.21	90.5
803	8031773	9.4	1.5	8.9	15.0	0.4	0.4	10.7	64.3	0.09	714.4
803	8031791	14.5	2.1	16.0	10.0	0.5	0.4	7.0	45.1	0.17	265.3
803	8031801	3.5	1.2	7.0	3.1	0.6	0.4	4.9	75.8	0.25	303.2
803	8031812	7.9	1.2	9.1	6.2	0.5	0.4	6.0	87.1	0.33	263.9
803	8031823	8.7	1.8	13.5	5.5	0.6	0.4	6.5	98.4	0.41	240.0
803	8031843	7.4	2.2	11.1	4.2	0.4	0.4	9.6	83.2	0.41	205.3
803	8031863	8.6	1.9	12.7	5.1	0.5	0.4	6.3	67.9	0.40	169.8
803	8031883	12.6	2.4	20.0	9.3	0.5	0.4	7.2	70.8	0.29	244.1
803	8031903	8.9	1.8	15.2	4.9	0.5	0.4	7.5	93.8	0.33	284.2
803	8031918	11.8	1.9	18.8	11.1	0.5	0.4	9.4	63.1	0.22	286.8
803	8031939	7.1	2.3	16.4	5.8	0.5	0.5	7.3	85.6	0.17	503.5
803	8031959	1.2	1.0	5.6	4.4	0.5	0.6	5.2	79.4	0.20	397.0
803	8031979	5.6	1.1	7.6	3.8	0.5	0.6	3.7	76.0	0.14	542.9
803	8031999	6.4	0.9	6.0	3.6	0.3	0.6	3.5	41.0	0.14	292.9
803	8032013	3.0	1.1	6.6	2.4	0.3	0.6	3.6	38.2	0.13	293.8
803	8032027	1.6	0.9	1.9	0.6	0.4	0.8	1.6	18.9	0.12	157.5
803	8032047	1.3	0.8	2.3	1.1	0.4	0.7	2.3	17.5	0.15	116.7
803	8032074	1.1	0.9	6.9	3.2	0.4	0.6	2.8	49.0	0.12	408.3
803	8032094	1.8	1.2	4.9	1.1	0.5	0.5	4.5	56.3	0.24	234.6
803	8032107	2.2	1.3	12.2	4.0	0.5	0.4	9.2	74.5	0.17	438.2
803	8032127	0.3	1.3	17.1	1.4	0.4	0.3	9.4	63.3	0.26	243.5
803	8032147	0.1	1.9	12.3	3.4	0.4	0.3	9.7	86.3	0.19	454.2
803	8032167	34.9	3.4	30.4	16.9	0.4	0.4	5.9	51.0	0.18	283.3
803	8032187	12.5	2.1	18.8	7.3	0.5	0.5	3.8	36.2	0.15	241.3
803	8032204	5.4	1.8	13.8	6.7	0.4	0.3	6.7	78.3	0.26	301.2
803	8032246	15.7	2.3	16.2	6.2	0.5	0.4	8.7	55.5	0.09	616.7
803	8032266	18.6	2.8	21.2	7.3	0.5	0.3	13.1	40.2	0.07	574.3
803	8032286	21.7	2.6	26.8	12.5	0.5	0.3	11.3	52.0	0.06	866.7
803	8032317	14.8	1.8	20.7	10.0	0.6	0.3	6.1	70.3	0.18	390.6
803	8032340	9.0	2.6	16.9	7.1	0.5	0.3	6.8	109.8	0.15	732.0
803	8,032,360	7.5	2.2	18.2	6.4	0.5	0.3	6.2	92.6	0.43	215.3

Table 4 Enrichment factors (EFs), Hg, TOC and Hg/TOC for samples of two sections in wells 570 and 803 from eastern and western (respectively) corners of the Bakchar ironstone deposit *(Continued)*

Well	Samples	Mo EF	U EF	V EF	P EF	Ti EF	Al EF	Fe EF	Hg, ppb	TOC, %	Hg/TOC
803	8032380	3.5	1.3	4.7	5.2	0.7	0.4	1.9	146.7	0.19	772.1

interval underlying the Kolpashevo ironstone. The Coniacian Narym ironstone in well 570 (Fig. 6) exhibits a sharp increase in U EF from 2.1 to 2.6. Because of the greater depth in the eastern part compared to that of the western part of the ironstone deposit (Fig. 2), the hypoxic seawater was more extensive in the former.

While the accumulation of chamosite-goethite ooids and different cements reflect a change in the geochemical environment from oxic to anoxic conditions during formation of ironstones (Rudmin et al. 2019). It is characterized by sequential formations of goethite-chamosite ooids, glauconite, berthierine or chamosite, pyrite and/or siderite. Narym and Kolpashevo ironstones encompassing hypoxic intervals consist of different mineral assemblages such as chamosite/glauconite + berthierine + goethite ± siderite ± occasional large pyrite and chamosite + glauconite + siderite + tiny pyrite, respectively.

Total content of REEs increases in ironstone intervals and decreases slightly in hypoxic intervals in both wells. The Coniacian and Santonian sediments usually exhibit higher LREE/HREE ratios (average of 15.3) relative to those in the Campanian and Paleocene (average of 13.3) (Figs. 6 and 7). Sediments representing hypoxic intervals as well as goethite-chamosite ironstones exhibit positive Ce anomaly, caused by the oxidation of cerium and its precipitation as iron oxyhydroxide and/or aluminosilicate (Bau 1999; Kraemer et al. 2017). Hypoxic intervals in the Narym and Kolpashevo ironstones, however, exhibit negative Eu anomaly. The negative Eu and Y anomalies are similar to those exhibited by low-temperature hydrothermal fluids (Bau and Dulski 1999; Sylvestre et al. 2017). Enhanced hydrothermal activity possibly led to the extensive emission of iron and methane saturated fluids and induced hypoxia on shelf of the West Siberian Sea. Redox sensitive proxies, REEs patterns, pyrite framboids as well as chamosite-pyrite-siderite mineral assemblages of ironstones indicate hypoxic bottom water condition. Hypoxic intervals in the Narym and Kolpashevo ironstones correspond to global geological events such as OAE-2 and OAE-3, respectively. Therefore, the formation of ooidal ironstones is closely associated with periods of oceanic hypoxia.

5.2 Relationship between ooidal ironstone formation, hypoxia, global volcanism and rifting

Several intervals such as in the Turonian, the early Santonian, the Santonian-Campanian boundary, the early Maastrichtian and the Maastrichtian-Paleocene boundary in the sections of the western and eastern parts of the deposit are marked by high contents of mercury (both Hg and Hg/TOC). Peaks of Hg and Hg/TOC patterns precede or coincide with the Coniacian and Santonian hypoxic intervals. Higher values of Hg and Hg/TOC in well 803 than in well 507 relates to closeness of the exhalation site in case of former. Ore bodies in the western part of the deposit (well 803) occur close to the tectonic uplift and therefore remain close to the exhalation site. Hg anomalies in the Meso-Cenozoic sediments of the West Siberian Sea correlated with the volcanisms of LIPs (such as Greater Ontong-Java Plateau, Karoo-Ferrar Province, High Arctic Province, and Deccan Traps) occurred in the Cenomanian-Turonian, the Campanian, the Maastrichtian-Paleocene (Ernst and Youbi 2017). The close correspondence between Hg anomalies and hypoxic intervals within the Meso-Cenozoic ironstone deposit in West Siberian Sea establishes the relationship between LIPs and OAEs (cf. Percival et al. 2015, 2018; Ernst and Youbi 2017; Scaife et al. 2017; Them et al. 2019). These large volcanic events possibly contributed to the formation of extensive ironstone ore deposits on ocean floor (cf. Van Houten and Arthur 1989; Percival et al. 2015; Ernst and Youbi 2017; Song et al. 2017).

Intense accumulation of ooidal ironstone might take place soon after an oceanic hypoxia (cf. Van Houten and Arthur 1989; McLaughlin et al. 2012; Bekker et al. 2014). Underwater exhalations of iron-saturated fluids would intensify during global volcanic events. Increase in bioproductivity and related marine hypoxia results in abundant ferrous iron in shelf waters (cf. Homoky 2017; Konhauser et al. 2017). The immobilization of this iron as silicates causes the accumulation of chamosite/glauconite-siderite-pyrite ironstones, as in the Narym and Kolpashevo ironstones. While the exhalation of fluids in oxic conditions leads to the rapid precipitation of iron as oxyhydroxides (goethite, lepidocrocite) as in the Bakchar ironstone deposit (Kimberley 1989; Sturesson et al. 2000; Rudmin et al. 2019). Global volcanic events possibly triggered the hydrothermal convection in continental rift systems of the West Siberian Plate (Surkov 2002; Saraev et al. 2011; Vibe et al. 2018). Metal-saturated aqueous fluids moved into the near-bottom waters through convection, similar to the continental rift system of the Dead Sea (Dill et al. 2010), or through underwater exhalation similar to the system of Mahengetang (Heikoop et al. 1996), the Hawaiian Islands (Hearty et al. 2010)

Table 5 Rare earth elements + Y (both in ppm) and geochemical parameters for samples of two sections in wells 570 and 803 from eastern and western (respectively) corners of the Bakchar ironstone deposit

Well	Samples	La	Ce	Pr	Nd	Sm	Eu	Gd	Tb	Dy	Ho	Er	Tm	Yb	Lu	Y	ΣREEs	LREE/ HREE	Ce/Ce*	Eu/Eu*
570	5701923	41	104	11.4	42.4	10.4	2.3	9.9	1.4	7.9	1.6	4.3	0.5	3.9	0.6	32	241.9	11.0	1.1	1.0
570	5701935	57	142	16.1	61.6	13.3	2.9	14.4	2.1	11.4	2.1	5.3	0.8	5.3	0.7	37	334.9	11.1	1.1	1.0
570	5701946	73	190	20.4	78.0	20.0	3.2	18.0	2.7	13.0	2.6	6.8	0.8	5.5	0.8	45	434.8	12.5	1.1	0.8
570	5701960	70	180	19.3	75.1	18.9	3.0	17.3	2.6	12.3	2.5	6.6	0.7	5.4	0.8	43	414.7	12.4	1.1	0.8
570	5701973	58	151	17.0	62.6	15.2	3.3	14.4	2.2	11.4	2.1	5.2	0.8	5.2	0.7	34	349.3	11.7	1.1	1.1
570	5701985	65	170	19.0	74.1	16.1	3.7	17.3	2.4	12.3	2.1	5.5	0.7	4.9	0.7	39	393.9	12.7	1.1	1.0
570	5701998	57	151	16.1	62.6	15.2	3.3	15.4	2.2	10.4	1.9	5.2	0.6	4.5	0.5	31	346.2	12.6	1.1	1.0
570	5702013	65	180	19.1	72.2	17.0	3.7	15.4	2.4	12.3	2.3	5.0	0.7	4.6	0.9	36	400.1	13.1	1.2	1.1
570	5702028	65	170	18.8	78.0	17.0	4.2	16.4	2.5	14.2	2.2	6.2	1.0	6.0	0.7	40	402.1	11.2	1.1	1.2
570	5702042	56	151	17.0	62.6	15.2	3.4	15.4	2.4	12.3	2.0	5.7	0.9	5.9	0.9	40	351.1	10.6	1.1	1.0
570	5702082	40	104	12.3	50.1	12.3	2.6	13.5	1.8	10.4	2.0	5.3	0.7	5.2	0.7	33	261.5	9.0	1.1	1.0
570	5702087	51	125	15.5	60.0	14.5	3.0	15.0	2.3	12.5	2.4	6.3	0.9	5.6	0.8	39	314.1	9.3	1.0	1.0
570	5702097	57	132	17.0	65.5	15.2	3.0	15.4	2.5	13.3	2.6	6.9	0.9	5.7	0.8	41	338.0	9.4	1.0	0.9
570	5702105	40	104	12.3	52.0	12.3	2.7	13.5	1.9	10.4	2.1	4.8	0.7	4.7	0.6	36	262.7	9.4	1.1	1.0
570	5702122	59	160	19.0	77.0	17.0	3.9	18.0	2.4	13.5	2.5	5.6	0.8	5.7	0.7	46	384.6	11.3	1.1	1.0
570	5702136	72	199	23.7	96.3	19.9	4.6	21.2	2.8	15.2	2.6	6.0	0.8	6.4	0.8	51	471.1	12.7	1.1	1.1
570	5702140	45	123	12.3	57.8	10.4	2.2	11.6	1.4	8.2	1.6	3.7	0.4	3.3	0.6	26	281.7	13.6	1.2	0.9
570	5702157	61	170	18.5	76.0	15.0	3.1	15.5	2.1	10.9	2.1	4.9	0.7	4.4	0.7	36	384.8	14.0	1.2	0.9
570	5702161	72	199	22.7	88.6	18.0	3.6	18.3	2.6	12.3	2.5	5.8	0.8	5.3	0.7	43	452.2	14.0	1.1	0.9
570	5702170	71	200	22.0	85.3	18.0	3.6	18.5	2.6	12.5	2.5	5.8	0.9	5.2	0.7	43	448.3	13.8	1.2	0.9
570	5702189	67	190	20.0	78.5	17.0	3.5	18.0	2.5	12.0	2.5	5.6	0.9	5.1	0.7	42	422.5	13.6	1.2	0.9
570	5702195	56	161	15.2	62.6	14.2	2.9	16.4	2.1	10.4	2.2	4.9	0.7	4.6	0.6	36	353.5	12.8	1.3	0.9
570	5702200	59	165	16.5	66.0	14.5	3.3	18.7	2.5	12.5	2.3	6.0	0.9	5.3	0.7	44	372.5	11.4	1.2	0.9
570	5702218	57	151	16.1	64.5	13.3	3.3	19.5	2.6	13.3	2.2	6.7	0.9	5.7	0.8	46	357.1	10.1	1.1	0.9
570	5702219	58	160	16.5	67.0	14.0	3.5	19.2	2.7	14.0	2.4	6.8	1.0	6.0	0.9	47	371.3	10.0	1.2	1.0
570	5702234	54	151	15.2	64.5	13.3	3.3	17.3	2.6	13.3	2.4	6.4	0.8	6.0	0.9	43	351.3	9.8	1.2	1.0
570	5702240	52	151	15.2	62.6	14.2	2.9	16.4	2.6	12.3	2.6	6.4	0.8	5.2	0.7	43	345.3	10.3	1.2	0.9
570	5702248	49	132	13.3	56.8	12.3	2.9	15.4	2.2	9.6	2.2	5.1	0.6	5.3	0.8	41	308.1	10.9	1.2	1.0
570	5702279	68	237	20.8	79.9	18.9	4.3	21.2	3.2	16.1	3.0	7.8	1.1	7.7	0.9	56	489.8	11.3	1.4	1.0
570	5702286	55	170	17.0	63.6	12.3	2.7	12.5	1.7	8.1	1.4	3.8	0.5	3.2	0.4	31	352.5	17.4	1.3	1.0
570	5702320	66	227	21.8	80.9	18.0	3.6	18.3	2.5	12.3	2.0	5.9	0.7	5.6	0.7	42	465.9	14.6	1.4	0.9
570	5702343	59	199	18.0	74.1	15.2	3.3	13.5	1.5	8.2	1.2	3.3	0.4	2.8	0.4	26	399.4	21.4	1.4	1.1
570	5702348	62	200	19.0	74.5	15.0	3.2	14.5	1.7	8.9	1.3	3.3	0.4	2.7	0.4	28	406.4	20.7	1.3	1.0
570	5702355	60	180	18.0	69.3	13.3	2.6	14.4	1.7	8.6	1.4	3.1	0.4	2.5	0.4	27	375.2	19.8	1.3	0.9
570	5702368	65	189	18.0	71.3	15.2	3.3	16.4	2.2	9.9	1.7	5.0	0.6	4.7	0.6	47	403.7	15.3	1.3	1.0
570	5702390	51	151	14.2	57.8	12.3	2.6	11.6	1.5	8.2	1.6	3.9	0.5	3.3	0.5	29	320.5	15.4	1.3	1.0
570	5702395	39	123	11.4	49.1	10.4	1.9	9.6	1.3	6.5	1.3	3.1	0.4	2.3	0.3	23	260.0	16.3	1.3	1.0
570	5702423	98	322	28.9	106.9	24.6	5.5	25.0	3.8	17.0	3.1	8.2	1.1	7.4	1.0	61	652.4	14.7	1.4	1.0
570	5702432	91	303	27.1	99.3	22.8	5.1	23.0	3.3	15.9	2.8	7.4	1.1	6.5	0.9	56	608.0	15.1	1.4	1.1
570	5702440	79	265	23.8	87.5	19.5	4.5	20.0	2.8	13.7	2.4	6.2	0.9	5.6	0.8	47	531.4	15.5	1.4	1.1
570	5702463	54	180	16.1	61.6	12.3	2.9	13.5	1.5	8.9	1.5	3.8	0.6	3.5	0.5	28	360.4	16.8	1.4	1.1
570	5702465	42	133	12.3	46.5	10.0	2.3	10.4	1.3	7.0	1.3	3.4	0.5	3.2	0.5	27	272.4	15.0	1.4	1.0
570	5702470	34	104	9.9	37.8	8.5	1.8	8.6	1.1	5.8	1.1	3.1	0.5	2.9	0.5	25	219.5	13.7	1.3	1.0

Table 5 Rare earth elements + Y (both in ppm) and geochemical parameters for samples of two sections in wells 570 and 803 from eastern and western (respectively) corners of the Bakchar ironstone deposit *(Continued)*

Well	Samples	La	Ce	Pr	Nd	Sm	Eu	Gd	Tb	Dy	Ho	Er	Tm	Yb	Lu	Y	ΣREEs	LREE/ HREE	Ce/Ce*	Eu/Eu*
570	5702480	26	71	7.1	27.9	6.6	1.3	6.5	0.9	4.4	1.0	2.7	0.4	2.7	0.4	22	158.9	11.8	1.2	0.9
570	5702488	31	89	8.7	33.4	7.8	1.6	7.7	1.0	5.2	1.1	2.9	0.4	2.8	0.5	24	193.1	12.9	1.3	1.0
803	8031624	28	87	8.1	31.0	6.0	1.5	6.8	1.1	6.3	1.2	3.5	0.4	3.2	0.4	12	184.5	10.5	1.3	1.1
803	8031634	77	190	22.0	95.0	20.0	4.5	20.0	3.0	17.0	2.6	6.5	0.9	7.0	1.1	57	466.6	11.3	1.1	1.1
803	8031645	78	200	24.0	99.0	21.0	4.7	21.0	3.0	16.0	2.6	7.0	1.1	7.2	1.0	58	485.6	11.8	1.1	1.1
803	8031665	70	180	22.0	84.0	17.0	4.2	23.0	3.2	16.0	2.4	6.8	0.9	5.6	0.8	48	435.9	11.2	1.1	1.0
803	8031682	14	58	7.5	37.0	9.1	2.3	11.0	1.9	10.0	1.8	5.1	0.8	4.5	0.6	21	163.6	5.6	1.2	1.1
803	8031702	15	52	8.6	30.0	8.4	2.2	11.0	2.1	9.6	1.9	4.5	0.8	4.1	0.7	20	150.8	5.4	1.0	1.1
803	8031712	74	190	24.0	90.0	21.0	4.0	23.0	3.6	17.0	2.8	7.2	1.1	6.9	1.0	53	465.6	10.8	1.0	0.9
803	8031722	80	200	23.0	98.0	18.0	5.3	25.0	3.4	17.0	2.7	7.9	1.2	6.7	1.0	53	489.2	11.3	1.1	1.1
803	8031736	63	150	18.0	72.0	17.0	3.4	20.0	2.5	13.0	2.0	6.0	1.0	5.5	0.9	41	374.3	11.1	1.0	0.9
803	8031753	50	130	15.0	61.0	12.0	3.1	16.0	2.1	11.0	1.4	3.6	0.7	3.9	0.6	35	310.3	12.4	1.1	1.0
803	8031773	36	90	10.0	37.0	7.9	2.2	9.8	1.3	6.6	1.1	2.7	0.3	2.6	0.4	22	207.9	12.9	1.1	1.2
803	8031791	55	140	16.0	60.0	13.0	3.3	15.0	2.3	11.0	1.9	5.3	0.7	4.3	0.6	36	328.4	11.6	1.1	1.1
803	8031801	35	88	10.0	38.0	7.0	2.2	10.0	1.3	6.0	1.0	3.0	0.4	2.3	0.4	22	204.6	13.3	1.1	1.2
803	8031812	41	93	11.0	48.0	9.4	2.0	11.0	1.7	7.2	1.0	2.9	0.5	2.6	0.5	24	231.7	13.2	1.0	0.9
803	8031823	47	130	14.0	58.0	12.0	2.7	12.0	1.7	8.3	1.3	3.7	0.6	3.2	0.5	29	295.0	14.3	1.2	1.1
803	8031843	45	120	13.0	55.0	11.0	2.5	11.0	1.4	7.8	1.3	3.8	0.5	3.4	0.4	29	276.1	13.8	1.1	1.1
803	8031863	53	140	16.0	65.0	12.0	3.1	13.0	1.7	8.7	1.5	5.0	0.6	4.6	0.6	37	324.7	13.3	1.1	1.2
803	8031883	76	200	22.0	95.0	20.0	4.3	20.0	2.6	14.0	2.4	6.2	0.9	5.6	0.7	49	469.7	13.5	1.1	1.0
803	8031903	70	180	20.0	83.0	16.0	3.7	16.0	2.2	10.0	1.7	5.0	0.7	3.5	0.6	36	412.4	16.4	1.1	1.1
803	8031918	68	180	20.0	83.0	17.0	3.5	20.0	2.6	12.0	1.8	5.4	0.8	4.6	0.7	40	419.3	14.1	1.1	0.9
803	8031939	85	220	24.0	95.0	20.0	4.0	19.0	2.3	11.0	1.9	5.1	0.8	4.3	0.7	37	493.2	17.9	1.1	1.0
803	8031959	50	150	14.0	59.0	11.0	2.2	13.0	1.5	6.1	1.2	2.2	0.4	2.3	0.4	22	313.3	21.3	1.3	0.9
803	8031979	60	170	16.0	70.0	14.0	2.8	13.0	1.8	8.3	1.4	3.0	0.5	3.0	0.5	27	364.3	18.7	1.3	1.0
803	8031999	49	130	13.0	56.0	11.0	2.3	12.0	1.5	5.8	1.1	3.1	0.4	2.8	0.4	23	288.4	18.1	1.2	0.9
803	8032013	54	150	16.0	62.0	12.0	2.7	12.0	1.8	6.9	1.0	3.1	0.6	2.4	0.3	24	324.8	19.2	1.2	1.1
803	8032027	48	130	13.0	54.0	9.5	2.1	9.3	1.2	5.5	0.8	2.1	0.3	2.2	0.3	20	278.3	21.5	1.2	1.1
803	8032047	54	170	15.0	58.0	13.0	2.4	10.0	1.1	4.9	0.9	2.1	0.2	1.7	0.2	17	333.6	28.8	1.4	1.0
803	8032074	58	150	15.0	72.0	14.0	2.8	11.0	1.6	6.9	1.0	2.6	0.4	2.4	0.4	26	338.2	21.0	1.2	1.1
803	8032094	42	110	12.0	46.0	9.3	1.8	12.0	1.3	5.1	0.9	2.1	0.3	1.8	0.3	19	244.9	19.8	1.1	0.8
803	8032107	35	98	9.8	40.0	7.7	1.6	7.9	1.0	5.0	1.0	2.1	0.3	2.0	0.3	18	211.6	17.2	1.2	1.0
803	8032127	36	110	10.0	38.0	9.6	1.8	9.0	1.2	5.5	0.9	2.0	0.3	1.5	0.4	18	226.2	18.2	1.3	0.9
803	8032147	34	89	9.4	33.0	7.2	1.3	8.9	1.0	5.0	0.8	1.9	0.3	1.9	0.3	18	194.0	16.3	1.1	0.8
803	8032167	90	220	27.0	100.0	23.0	5.1	27.0	3.8	19.0	2.9	8.6	1.4	7.1	1.2	65	536.1	11.2	1.0	1.0
803	8032187	69	170	21.0	75.0	18.0	4.2	21.0	3.3	14.0	2.5	5.7	0.7	6.0	0.9	46	411.3	11.4	1.0	1.0
803	8032204	62	170	18.0	63.0	12.0	2.8	13.0	1.6	7.2	1.2	3.2	0.3	2.3	0.4	26	357.0	21.0	1.2	1.1
803	8032246	70	200	21.0	83.0	17.0	3.4	17.0	2.3	9.9	1.8	4.8	0.7	4.1	0.7	33	435.7	17.0	1.2	0.9
803	8032266	54	170	16.0	56.0	12.0	2.7	13.0	1.9	8.2	1.3	3.5	0.5	3.0	0.5	26	342.6	17.1	1.3	1.0
803	8032286	55	180	17.0	64.0	12.0	3.0	13.0	2.0	8.5	1.5	3.8	0.6	3.5	0.5	26	364.4	16.9	1.3	1.1
803	8032317	46	160	15.0	56.0	12.0	2.2	11.0	1.6	6.5	1.1	3.0	0.5	2.8	0.4	22	318.0	19.1	1.4	0.9
803	8032340	37	120	12.0	44.0	9.6	2.3	10.0	1.3	6.6	1.0	3.1	0.5	2.7	0.4	19	250.5	15.1	1.3	1.1
803	8032360	41	130	13.0	47.0	9.3	2.4	10.0	1.3	6.7	1.0	2.6	0.4	2.3	0.4	19	267.3	17.3	1.3	1.2

Table 5 Rare earth elements + Y (both in ppm) and geochemical parameters for samples of two sections in wells 570 and 803 from eastern and western (respectively) corners of the Bakchar ironstone deposit *(Continued)*

Well	Samples	La	Ce	Pr	Nd	Sm	Eu	Gd	Tb	Dy	Ho	Er	Tm	Yb	Lu	Y	ΣREEs	LREE/ HREE	Ce/Ce*	Eu/Eu*
803	8032380	22	57	5.8	23.0	4.1	1.0	4.5	0.6	3.0	0.6	1.6	0.2	1.3	0.2	16	124.8	15.7	1.2	1.1

and Trinidad Island (Kimberley 1994). The methane fluid degassing possibly accompanied the intensive removal of iron and the formation of ironstones in the geological past (cf. Rudmin et al. 2018).

6 Conclusions

Based on the studies of pyrite framboids and major and trace elements concentrations in core samples collected from the two wells penetrating the ironstone deposits in western Siberia, we can draw the following conclusions:

1) Pyrite of different sizes occurs in various morphological forms such as framboids, irregular and subhedral masses, and euhedral crystals. Variation in diameter of pyrite framboids reveals three hypoxic intervals within the Meso-Cenozoic Bakchar ironstone deposit in western Siberia.

2) Occurrences of ooidal ironstone correspond to the three hypoxic intervals in the middle Coniacian, the Santonian, and the early Campanian. Trace element enrichment factors exhibit sharp swings in these intervals. Narym and Kolpashevo ironstones encompassing the hypoxic intervals reflect to different mineral assemblages and geochemistry. Therefore the formation of ooidal ironstone is closely linked to the hypoxic shelf water.

3) Enhanced hydrothermal activity resulted in low-temperature fluid emissions and induced oceanic hypoxia

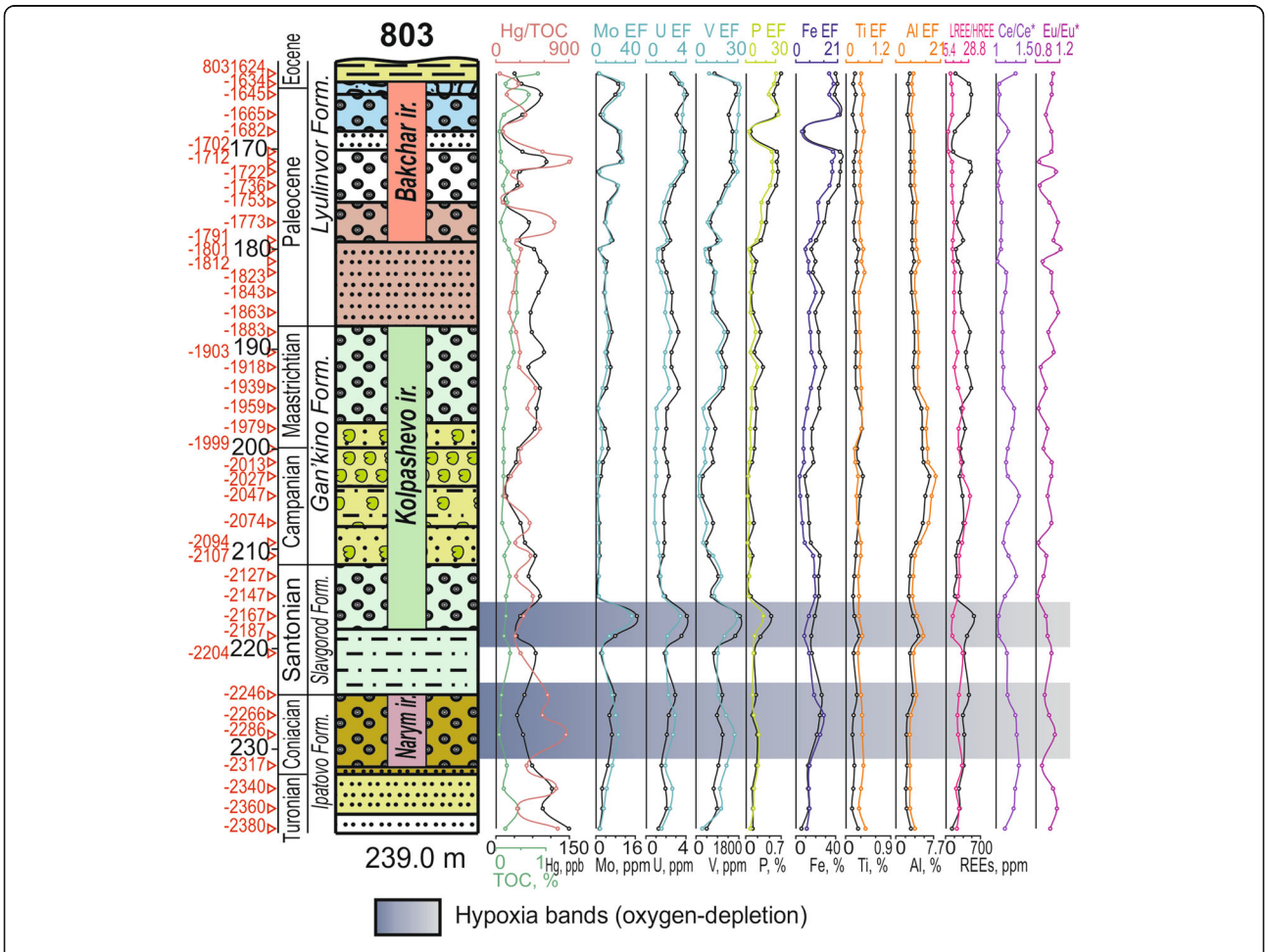

Fig. 7 Lithostratigraphic column for well 803 showing geochemical profiles of TOC, Hg, Hg/TOC, elemental enrichment factors (EFs). Correlation between high content of TOC, Hg/TOC, and elevated enrichment factors of Mo, U, V indicates two hypoxic intervals (marked by light grey shades). Paucity of pyrite framboids rules out hypoxia in the Maastrichtian-Paleocene sequences. *Form.* = Formation; *ir.*= ironstone

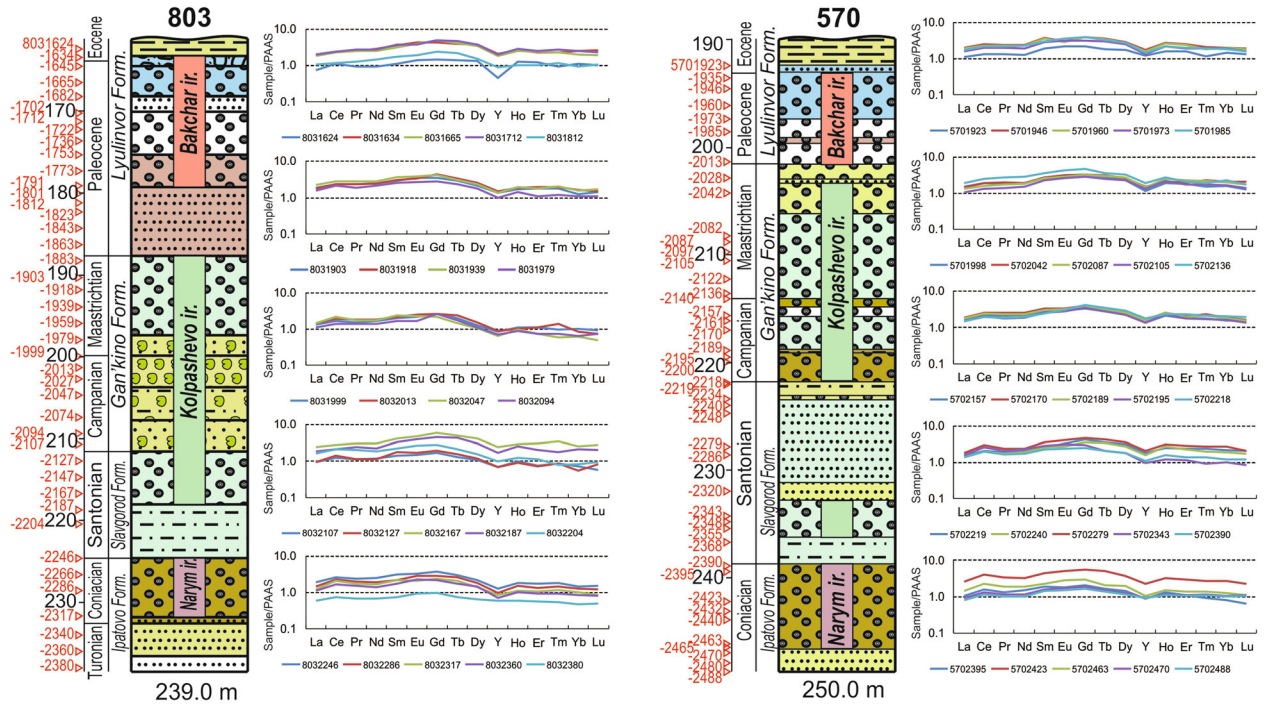

Fig. 8 Variations of REEs patterns through the stratigraphic sequences in wells 570 and 803 from eastern and western (respectively) corners of the Bakchar ironstone deposit. Hypoxic intervals in the Narym and Kolpashevo ironstones exhibit negative Eu and Y anomalies, indicating influence of low-temperature hydrothermal fluids

during the formation of ironstones in Bakchar ironstone deposit. Redox sensitive proxies, pyrite framboids and ore mineral assemblages record the hydrothermal activation.

4) Mercury anomalies characterize hypoxic intervals, which were contemporaneous with global volcanic events. Thus, a potential geological connection is established between LIPs, OAEs and ooidal ironstone deposits. Hydrothermal exhalation associated with rifting contributes iron for the ooidal ironstone deposits.

Abbreviations

EF: Enrichment factor; ICP-MS: Inductively coupled plasma-mass spectrometry; LIPs: Large Igneous Provinces; OAE: Ocean anoxic event; REEs: Rare earth elements; SEM: Scanning electron microscope; TEs: Trace elements; TOC: Total organic carbon; XRF: X-ray fluorescence microscope

Acknowledgements

The authors thank the anonymous reviewers and editors for their suggestions and revisions, which improved the paper.

Authors' contributions

MR and AM conceived and designed the study. MR and AR collected the materials. MR, EF, EL, RK, and AR performed the laboratory investigations. MR, SB, EA and AM analyzed the data. SB and EA helped modify the manuscript. MR and SB wrote the paper. All authors read and approved the final manuscript.

Funding

Laboratory geochemical investigations were carried out at National Research Tomsk Polytechnic University within the framework of a Competitiveness Enhancement Program Grant (Project VIU-OG-61/2019). The mineralogical part of research was funded by Russian Foundation for Basic Research and Tomsk Region (19–45-703002).

Availability of data and materials

All data generated or analyzed during this study are included in this published article.

Competing interests

The authors declare that they have no competing interests.

Author details

[1]Division for Geology, School of Earth Sciences and Engineering, Tomsk Polytechnic University, 634050 Tomsk, Russia. [2]Department of Earth Sciences, Indian Institute of Technology Bombay, Powai, Mumbai 400076, Maharashtra, India. [3]Department of Geoscience, French-Azerbaijani University (UFAZ), AZ1000 Baku, Azerbaijan. [4]Institute of Monitoring of Climatic and Ecological System of SB of RAS, 634055 Tomsk, Russia.

Received: 1 May 2019 Accepted: 11 November 2019
Published online: 01 January 2020

References

Algeo, T.J., and N. Tribovillard. 2009. Environmental analysis of paleoceanographic systems based on molybdenum–uranium covariation. *Chemical Geology* 268: 211–225.

Aller, R.C., J.E. Mackin, and R.T. Cox. 1986. Diagenesis of Fe and S in Amazon inner shelf muds: Apparent dominance of Fe reduction and implications for the genesis of ironstones. *Continental Shelf Research* 6: 263–289.

Arthur, M.A., W.E. Dean, and L.M. Pratt. 1988. Geochemical and climatic effects of increased marine organic carbon burial at the Cenomanian/Turonian boundary. *Nature* 335: 714–717.

Asochakova, E. 2014. Clay minerals of oolitic iron ores from the Bakchar deposit (Western Siberia). In: *International multidisciplinary scientific geoconference, surveying geology and mining ecology management* (SGEM), pp. 859–866.

Bau, M. 1999. Scavenging of dissolved yttrium and rare earths by precipitating iron oxyhydroxide: Experimental evidence for Ce oxidation,

Y-ho fractionation, and lanthanide tetrad effect. *Geochimica et Cosmochimica Acta* 63: 67–77.

Bau, M., and P. Dulski. 1999. Comparing yttrium and rare earths in hydrothermal fluids from the mid-Atlantic ridge: Implications for Y and REE behaviour during near-vent mixing and for the Y/ho ratio of Proterozoic seawater. *Chemical Geology* 155: 77–90.

Bekker, A., N.J. Planavsky, B. Krapež, B. Rasmussen, A. Hofmann, J.F. Slack, O.J. Rouxel, and K.O. Konhauser. 2014. Iron formations: their origins and implications for ancient seawater chemistry. In *Treatise on geochemistry*, ed. H. Holland and K. Turekian, 561–628. Amsterdam: Elsevier. https://doi.org/10.1016/B978-0-08-095975-7.00719-1.

Belous, N.C., I.V. Nikolaeva, Y.P. Kazansky, A.P. Berdnikov, V.M. Klyarovskiy, V.P. Kuznetsov, and A.A. Babin. 1964. *The Western-Siberian iron ore basin*. Novosibirsk: Siberian Branch of the Academy of Sciences of the USSR (in Russia).

Berner, R.A. 1984. Sedimentary pyrite formation: An update. *Geochimica et Cosmochimica Acta* 48: 605–615.

Bond, D.P.G., and P.B. Wignall. 2010. Pyrite framboid study of marine Permian-Triassic boundary sections: A complex anoxic event and its relationship to contemporaneous mass extinction. *Bulletin of the Geological Society of America* 122: 1265–1279.

Brumsack, H.-J. 2006. The trace metal content of recent organic carbon-rich sediments: Implications for cretaceous black shale formation. *Palaeogeography, Palaeoclimatology, Palaeoecology* 232: 344–361.

Burkhalter, R.M. 1995. Ooidal ironstones and ferruginous microbialites: Origin and relation to sequence stratigraphy (Aalenian and Bajocian, Swiss Jura mountains). *Sedimentology* 42: 57–74.

Castano, J.R., and R.M. Garrels. 1950. Experiments on the deposition of iron with special reference to the Clinton iron ore deposits. *Economic Geology* 45: 755–770.

Dahanayake, K., and W. Krumbein. 1986. Microbial structures in oolitic iron formations. *Mineralium Deposita* 21: 85–94.

Di Bella, M., G. Sabatino, S. Quartieri, A. Ferretti, B. Cavalazzi, R. Barbieri, F. Foucher, F. Messori, and F. Italiano. 2019. Modern Iron Ooids of hydrothermal origin as a proxy for ancient deposits. *Scientific Reports* 9: 7107.

Dill, H.G., R. Botz, Z. Berner, and A.M.B. Abu Hamad. 2010. The origin of pre- and synrift, hypogene Fe-P mineralization during the Cenozoic along the Dead Sea transform fault, Northwest Jordan. *Economic Geology* 105: 1301–1319.

El-Habaak, G., M. Askalany, M. Faraghaly, and M. Abdel-Hakeem. 2016. The economic potential of El-Gedida glauconite deposits, El-Bahariya oasis, Western Desert, Egypt. *Journal of African Earth Sciences* 120: 186–197.

Ernst, R.E., and N. Youbi. 2017. How large igneous provinces affect global climate, sometimes cause mass extinctions, and represent natural markers in the geological record. *Palaeogeography, Palaeoclimatology, Palaeoecology* 478: 30–52.

Gnibidenko, Z.N., N.K. Lebedeva, and A.V. Levicheva. 2015. Magnetostratigraphy of the Campanian–Maastrichtian Bakchar Basin (southeastern West Siberia). *Russian Geology and Geophysics* 56: 1652–1661.

Hearty, P.J., J.M. Webster, D.A. Clague, D.S. Kaufman, J. Bright, J. Southon, and W. Renema. 2010. A pulse of ooid formation in Maui Nui (Hawaiian islands) during termination I. *Marine Geology* 268: 152–162.

Heikoop, J.M., C.J. Tsujita, M.J. Risk, T. Tomascik, and A.J. Mah. 1996. Modern iron ooids from a shallow-marine volcanic setting: Mahengetang, Indonesia. *Geology* 24: 759–762.

Homoky, W.B. 2017. Biogeochemistry: Deep ocean iron balance. *Nature Geoscience* 10: 162–164.

Huber, N.K., and R.M. Garrels. 1953. Relation of pH and oxidation potential to sedimentary iron mineral formation. *Economic Geology* 48: 337–357.

Jenkyns, H.C. 2010. Geochemistry of oceanic anoxic events. *Geochemistry, Geophysics, Geosystems* 11: 1–30.

Jones, M.M., D.E. Ibarra, Y. Gao, B.B. Sageman, D. Selby, C.P. Chamberlain, and S.A. Graham. 2018. Evaluating late cretaceous OAEs and the influence of marine incursions on organic carbon burial in an expansive east Asian paleo-lake. *Earth and Planetary Science Letters* 484: 41–52.

Keller, G., P. Mateo, J. Punekar, H. Khozyem, B. Gertsch, J. Spangenberg, A.M. Bitchong, and T. Adatte. 2018. Environmental changes during the cretaceous-Paleogene mass extinction and Paleocene-Eocene thermal maximum: Implications for the Anthropocene. *Gondwana Research* 56: 69–89.

Kholodov, V.N. 2014. Geochemical problems of the behavior of phosphorus: A basis for the biogenic hypothesis of phosphorite formation. *Lithology and Mineral Resources* 49: 228–249.

Kimberley, M.M. 1979. Origin of Oolitic Iron formations. *SEPM Journal of Sedimentary Research* 49: 111–131.

Kimberley, M.M. 1989. Exhalative origins of iron formations. *Ore Geology Reviews* 5: 13–145.

Kimberley, M.M. 1994. Debate about ironstone: Has solute supply been surficial weathering, hydrothermal convection, or exhalation of deep fluids? *Terra Nova* 6: 116–132.

Konhauser, K.O., N.J. Planavsky, D.S. Hardisty, L.J. Robbins, T.J. Warchola, R. Haugaard, S.V. Lalonde, C.A. Partin, P.B.H. Oonk, H. Tsikos, T.W. Lyons, A. Bekker, and C.M. Johnson. 2017. Iron formations: A global record of Neoarchaean to Palaeoproterozoic environmental history. *Earth-Science Reviews* 172: 140–177.

Kraemer, D., N. Tepe, O. Pourret, and M. Bau. 2017. Negative cerium anomalies in manganese (hydr) oxide precipitates due to cerium oxidation in the presence of dissolved siderophores. *Geochimica et Cosmochimica Acta* 196: 197–208.

Lebedel, V., C. Lezin, B. Andreu, M.-J. Wallez, E.M. Ettachfini, and L. Riquier. 2013. Geochemical and palaeoecological record of the Cenomanian–Turonian anoxic event in the carbonate platform of the Preafrican trough, Morocco. *Palaeogeography, Palaeoclimatology, Palaeoecology* 369: 79–98.

Lebedeva, N.K., G.N. Aleksandrova, B.N. Shurygin, M.N. Ovechkina, and Z.N. Gnibidenko. 2013. Paleontological and magnetostratigraphic data on upper cretaceous deposits from borehole no. 8 (Russkaya Polyana District, southwestern Siberia). *Stratigraphy and Geological Correlation* 21: 48–78.

Lebedeva, N.K., O.B. Kuzmina, E.S. Sobolev, and I.V. Khazina. 2017. Stratigraphy of upper cretaceous and Cenozoic deposits of the Bakchar iron ore deposit (southwestern Siberia): New data. *Stratigraphy and Geological Correlation* 25: 76–98.

Maynard, J.B. 1986. Geochemistry of oolitic iron ores, an electron microprobe study. *Economic Geology* 81: 1473–1483.

McLaughlin, P.I., P. Emsbo, and C.E. Brett. 2012. Beyond black shales: The sedimentary and stable isotope records of oceanic anoxic events in a dominantly oxic basin (Silurian; Appalachian Basin, USA). *Palaeogeography, Palaeoclimatology, Palaeoecology* 367–368: 153–177.

Merinero, R., and V. Cárdenes. 2018. Theoretical growth of framboidal and sunflower pyrite using the R-package frambgrowth. *Mineralogy and Petrology* 112: 577–589.

Merinero, R., R. Lunar, L. Somoza, V. Díaz-Del-Río, and J. Martínez-Frías. 2009. Nucleation, growth and oxidation of framboidal pyrite associated with hydrocarbon-derived submarine chimneys: Lessons learned from the Gulf of Cadiz. *European Journal of Mineralogy* 21: 947–961.

Merinero, R., V. Cárdenes, R. Lunar, M.N. Boone, and V. Cnudde. 2017. Representative size distributions of framboidal, euhedral, and sunflower pyrite from high-resolution X-ray tomography and scanning electron microscopy analyses. *American Mineralogist* 102: 620–631.

Nikolaeva, I.V. 1967. *Bakchar Oolitic Iron ore deposit*. Novosibirsk: Siberian Branch of the Academy of Sciences of the USSR (in Russia).

Núñez-Useche, F., C. Canet, R. Barragán, and P. Alfonso. 2016. Bioevents and redox conditions around the Cenomanian–Turonian anoxic event in Central Mexico. *Palaeogeography, Palaeoclimatology, Palaeoecology* 449: 205–226.

Pavlov, D.I. 1989. Relationship of sedimentary iron and manganese deposits with petroleum and gas-bearing basins. *Geology of Ore Deposits* 31: 80–91.

Pavlov, D.I. 1996. Oolitic iron-ore deposits: Supergene and catagenetic-sedimentary deposits. *Transactions (Doklady) of the Russian Academy of Sciences. Earth Science Sections* 343: 120–123.

Pavlov, D.I., D.I. Gorzhevskiy, G.A. Goleva, M.K. Kalinko, A.A. Kartsev, and A.V. Lipayeva. 1991. Conjunction of ore- and oil-forming systems in sedimentary basins and the prediction of ore deposits. *International Geology Review* 33: 822–829.

Percival, L.M.E., M.L.I. Witt, T.A. Mather, M. Hermoso, H.C. Jenkyns, S.P. Hesselbo, A.H. Al-Suwaidi, M.S. Storm, W. Xu, and M. Ruhl. 2015. Globally enhanced mercury deposition during the end-Pliensbachian extinction and Toarcian OAE: A link to the Karoo–Ferrar large Igneous Province. *Earth and Planetary Science Letters* 428: 267–280.

Percival, L.M.E., H.C. Jenkyns, T.A. Mather, A.J. Dickson, S.J. Batenburg, M. Ruhl, S.P. Hesselbo, R. Barclay, I. Jarvis, S.A. Robinson, and L. Woelders. 2018. Does large igneous province volcanism always perturb the mercury cycle? Comparing the records of oceanic anoxic event 2 and the end-cretaceous to other Mesozoic events. *American Journal of Science* 318: 799–860.

Petranek, J., and F.B. Van Houten. 1997. Phanerozoic ooidal ironstones. In *Czech Geological Survey Special Papers*, 4–71. Prague: Czech Geological Survey.

Podobina, V.M., and T.G. Kseneva. 2005. Upper cretaceous zonal stratigraphy of the west Siberian plain based on foraminifera. *Cretaceous Research* 26: 133–143.

Raven, M.R., D.A. Fike, M.L. Gomes, S.M. Webb, A.S. Bradley, and H.-L.O. McClelland. 2018. Organic carbon burial during OAE2 driven by changes in the locus of organic matter sulfurization. *Nature Communications* 9: 3409.

Rickard, D. 2019. How long does it take a pyrite framboid to form? *Earth and Planetary Science Letters* 513: 64–68.

Rudmin, M.A., and A.K. Mazurov. 2016. Oolitic ores in the Bakchar iron-ore cluster (Tomsk oblast). *Doklady Earth Sciences* 471: 1238–1241.

Rudmin, M., A. Mazurov, and L. Bolsunovskaya. 2014. Mineral and elemental composition features of "loose" oolitic ores in Bakchar iron ore cluster (Tomsk oblast). *IOP Conference Series: Earth and Environmental Science* 21: 1–6. https://doi.org/10.1088/1755-1315/21/1/012003.

Rudmin, M., A.P. Roberts, C.-S. Horng, A. Mazurov, O. Savinova, A. Ruban, R. Kashapov, and M. Veklich. 2018. Ferrimagnetic Iron sulfide formation and methane venting across the Paleocene-Eocene thermal maximum in shallow marine sediments, ancient west Siberian Sea. *Geochemistry, Geophysics, Geosystems* 19: 1–22.

Rudmin, M., A. Mazurov, and S. Banerjee. 2019. Origin of ooidal ironstones in relation to warming events: Cretaceous-Eocene Bakchar deposit, south-East Western Siberia. *Marine and Petroleum Geology* 100: 309–325.

Sabatino, N., S. Ferraro, R. Coccioni, M. Bonsignore, M. Del Core, V. Tancredi, and M. Sprovieri. 2018. Mercury anomalies in upper Aptian-lower Albian sediments from the Tethys realm. *Palaeogeography, Palaeoclimatology, Palaeoecology* 495: 163–170.

Saraev, S.V., T.P. Baturina, and A.V. Travin. 2011. Petrology, sedimentology, geochemistry, and absolute age of Triassic volcanosedimentary rocks from the southwest of the west Siberian geosyneclise (Kurgan region). *Russian Geology and Geophysics* 52: 871–887.

Sawlowicz, Z. 1993. Pyrite framboids and their development: A new conceptual mechanism. *Geologische Rundschau* 82: 148–156.

Scaife, J.D., M. Ruhl, A.J. Dickson, T.A. Mather, H.C. Jenkyns, L.M.E. Percival, S. P. Hesselbo, J. Cartwright, J.S. Eldrett, S.C. Bergman, and D. Minisini. 2017. Sedimentary mercury enrichments as a marker for submarine large Igneous Province volcanism? Evidence from the mid-Cenomanian event and oceanic anoxic event 2 (late cretaceous). *Geochemistry, Geophysics, Geosystems* 18: 4253–4275.

Schlanger, S.O., and H.C. Jenkyns. 1976. Cretaceous oceanic anoxic events: Causes and consequences. *Geologie en Mijnbouw* 55: 179–184.

Siehl, A., and J. Thein. 1989. *Minette-type ironstones*, 175–193. London: Phanerozoic Ironstones Geological Society Special Publication.

Song, H.H., G. Jiang, S.W. Poulton, P.B. Wignall, J. Tong, H.H. Song, Z. An, D. Chu, L. Tian, Z. She, and C. Wang. 2017. The onset of widespread marine red beds and the evolution of ferruginous oceans. *Nature Communications* 8: 399.

Strakhov, N.M. 1947. Iron ore Facies and their analogues in the Earth's history: Experience of historical-geographical analysis of sedimentary processes. *Trud IGN AN SSSR. Geology Series* 22.

Sturesson, U. 2003. Lower Paleozoic iron oolites and volcanism from a Baltoscandian perspective. *Sedimentary Geology* 159: 241–256.

Sturesson, U., J.M. Heikoop, and M.J. Risk. 2000. Modern and Palaeozoic iron ooids – A similar volcanic origin. *Sedimentary Geology* 136: 137–146.

Surkov, V.S. 2002. Neogean evolution of the young ural-Siberian platform. *Geologiya i Geofizika* 43: 754–761.

Sylvestre, G., N.T. Evine Laure, K.N. Gus Djibril, D.S. Arlette, M. Cyriel, N. Timoléon, and N. Jean Paul. 2017. A mixed seawater and hydrothermal origin of superior-type banded iron formation (BIF)-hosted Kouambo iron deposit, Palaeoproterozoic Nyong series, southwestern Cameroon: Constraints from petrography and geochemistry. *Ore Geology Reviews* 80: 860–875.

Taylor, K.G., and K.O. Konhauser. 2011. Iron in earth surface systems: A major player in chemical and biological processes. *Elements* 7: 83–88.

Them, T.R., C.H. Jagoe, A.H. Caruthers, B.C. Gill, S.E. Grasby, D.R. Gröcke, R. Yin, and J.D. Owens. 2019. Terrestrial sources as the primary delivery mechanism of mercury to the oceans across the Toarcian oceanic anoxic event (early Jurassic). *Earth and Planetary Science Letters* 507: 62–72.

Todd, S.E., P.K. Pufahl, J.B. Murphy, and K.G. Taylor. 2019. Sedimentology and oceanography of early Ordovician ironstone, Bell Island, Newfoundland: Ferruginous seawater and upwelling in the Rheic Ocean. *Sedimentary Geology* 379: 1–15.

Tribovillard, N., T.J. Algeo, T. Lyons, and A. Riboulleau. 2006. Trace metals as paleoredox and paleoproductivity proxies: An update. *Chemical Geology* 232: 12–32.

Tribovillard, N., T.J. Algeo, F. Baudin, and A. Riboulleau. 2012. Analysis of marine environmental conditions based on molybdenum–uranium covariation — Applications to Mesozoic paleoceanography. *Chemical Geology* 324: 46–58.

Turgeon, S.C., and R.A. Creaser. 2008. Cretaceous oceanic anoxic event 2 triggered by a massive magmatic episode. *Nature* 454: 323–326.

Van Houten, F.B. 1986. Search for Milankovitch patterns among oolitic ironstones. *Paleoceanography* 1: 459–466.

Van Houten, F.B., and M.A. Arthur. 1989. Temporal patterns among Phanerozoic oolitic ironstones and oceanic anoxia. *Geological Society Special Publication* 46: 33–49. https://doi.org/10.1144/GSL.SP.1989.046.01.06.

Van Houten, F.B., and D.P. Bhattacharyya. 1982. Phanerozoic Oolitic ironstones — Geologic record and Facies model. *Annual Review of Earth and Planetary Sciences* 10: 441–457. https://doi.org/10.1146/annurev.ea.10.050182.002301.

Van Houten, F.B., and M.E. Purucker. 1984. Glauconitic peloids and chamositic ooids – Favorable factors, constraints, and problems. *Earth-Science Reviews* 20: 211–243.

Vibe, Y., H.-P. Bunge, and S.R. Clark. 2018. Anomalous subsidence history of the west Siberian Basin as an indicator for episodes of mantle induced dynamic topography. *Gondwana Research* 53: 99–109.

Wagreich, M. 2012. "OAE 3" – Regional Atlantic organic carbon burial during the Coniacian–Santonian. *Climate of the Past* 8: 1447–1455. https://doi.org/10.5194/cp-8-1447-2012.

Wei, H., T.J. Algeo, H. Yu, J. Wang, C. Guo, and G. Shi. 2015. Episodic euxinia in the Changhsingian (late Permian) of South China: Evidence from framboidal pyrite and geochemical data. *Sedimentary Geology* 319: 78–97.

Wignall, P.B., R. Newton, and M.E. Brookfield. 2005. Pyrite framboid evidence for oxygen-poor deposition during the Permian–Triassic crisis in Kashmir. *Palaeogeography, Palaeoclimatology, Palaeoecology* 216: 183–188.

Wilkin, R.T., H.L. Barnes, and S.L. Brantley. 1996. The size distribution of framboidal pyrite in modern sediments: An indicator of redox conditions. *Geochimica et Cosmochimica Acta* 60: 3897–3912.

Young, T.P. 1989. Phanerozoic ironstones: An introduction and review. *Geological Society Special Publication* 46: ix–xxv. https://doi.org/10.1144/GSL.SP.1989.046.01.02.

Zhao, J., J. Liang, X. Long, J. Li, Q. Xiang, J. Zhang, and J. Hao. 2018. Genesis and evolution of framboidal pyrite and its implications for the ore-forming process of Carlin-style gold deposits, southwestern China. *Ore Geology Reviews* 102: 426–436.

Publisher's Note